TECHNISCHE UNIVERSITÄT WIEN
Vienna University of Technology

THE UNIVERSITY of NORTH CAROLINA at CHAPEL HILL

ENERGETICS AND EQUAL-TIME RESPONSE OF STRONGLY-COUPLED FERMIONS IN ONE AND TWO DIMENSIONS

DIPLOMARBEIT

Ausgeführt am

Institut für Festkörperphysik,
Technische Universität Wien

in Zusammenarbeit mit dem

Department of Physics and Astronomy,
University of North Carolina at Chapel Hill

unter Anleitung von

Associate Prof. Dr. Alessandro Toschi

und

Assistant Prof. Dr. Joaquín Drut

durch

Lukas Rammelmüller, 1026755.

Wien, am 9. Mai, 2016.

For Chri and Keili,
whom I owe this dedication.
You probably made me do this.

Abstract

Strongly interacting Fermi gases constitute a very challenging and interesting area within many-body physics and have received a tremendous amount of theoretical and experimental attention. Especially in the last decade, when it became possible to probe low-dimensional, ultracold atomic gases experimentally, many new approaches were developed to understand the physics of reduced dimensionality.
In this work, we set out to characterize the ground-state of interacting Fermi gases in one and two spatial dimensions. We calculate quantities across a wide range of interaction strengths and particle numbers, in order to characterize the crossover from few- to many-body physics. Although numerous methods exist to treat aspects of the one-dimensional (1D) case analytically, there currently is no known method to extract results from two-dimensional (2D) systems in such a way. We therefore need to address this problem numerically and choose to treat the problem by means of Quantum Monte Carlo (QMC) methods. Specifically, we calculate quantities on the lattice, using an auxiliary field decomposition, closely related to methods typically used in lattice-QCD calculations.
In the first part of this work, we introduce the physics of Fermi gases. Furthermore, we provide an overview of the necessary knowledge and definitions needed to understand this work. In the second chapter, the concept of stochastic integration is introduced. Starting at the basics of Monte Carlo integration, we arrive at the specific algorithms used in this work. Subsequently, we present results for the ground-state of 1D and 2D systems in chapters 3 and 4, respectively. We focus on equal-time density matrices as well as energetics in both cases. Finally, we conclude our work in the last chapter and point out possibilities to extend our research in the future.

Kurzfassung

Stark wechselwirkende Fermi-Gase verkörpern einen sehr anspruchsvollen und interessanten Teilbereich der Vielteilchenphysik. Aufgrund der vielfältigen Effekte haben diese Systeme enorme Aufmerksamkeit erhalten, sowohl theoretisch also auch experimentell. Durch die Weiterentwicklung experimenteller Techniken in den letzten zehn Jahren wurde es möglich, niedrigdimensionale Systeme zu untersuchen. Im Zuge dessen wurden viele neue Konzepte und Methoden entwickelt um die Physik hinter der reduzierten Dimensionalität zu verstehen.
Diese Arbeit beschreibt den Grundzustand wechselwirkender Fermi-Gase in ein und zwei räum- lichen Dimensionen. Wir führen Berechnungen für schwach bis stark gekoppelte Systeme durch und untersuchen zudem den Übergang von Wenig- zu Vielteilchenphysik. Während für den eindimensionalen Fall Methoden existieren, die es erlauben, Resultate analytisch zu berechnen, gibt es für zweidimensionale Systeme bis dato keine Möglichkeit, solche Berechnungen durchzufürhen. Aus diesem Grund sind wir an eine numerische Herangehensweise gebunden, welche in unserem Fall mit Quanten-Monte-Carlo (QMC) Methoden durchgeführt wird. Im Speziellen berechnen wir physikalische Größen auf einem Gitter und benützen eine Aufteilung der auftretenden Integrale mittels Hilfsfelder - eine Technik die aus Gitter-QCD Berechnungen bekannt ist.
Im ersten Teil dieser Arbeit werden wir in die Fermi-Gase einführen und deren einzigartige Eigenschaften diskutieren. Außerdem geben wir einen Überblick über die nötige Theorie, um die ge- zeigten Resultate zu verstehen. Im zweiten Kapitel wird das Konzept der stochastischen Integration beschrieben, beginnend mit grundlegenden Konzepten der Monte-Carlo Integration bis hin zu den speziellen Algorithmen, welche für diese Arbeit angewendet wurden. Nach dem theoretischen Teil zeigen wir Ergebnisse für den Grundzustand von 1D- und 2D-Systemen in den Kapiteln drei und vier. Wir präsentieren Einteilchen-Dichtematrizen und Impulsverteilungen für beide Fälle, außerdem Zweiteilchen-Dichtematrizen für eindimensionale Systeme. Für den zweidimensionalen Fall wird überdies die Grundzustands- und Wechselwirkungsenergie behandelt. Abschließend geben wir eine Zusammenfassung über die vorliegende Arbeit und diskutieren Möglichkeiten zur weiteren Behandlung fermionischer Systeme.

Acknowledgements

Looking back over the past six years lets me realize how much people contributed to the success of my studies in one way or another. In the first place, I want to thank my family for giving me the opportunity to study physics at all, supporting me with needed advice as well as financially and for providing a safe base throughout this endeavour. There is no hope I can do anything that really expresses how thankful I am for what you did for me.
When I came to Chapel Hill for an exchange semester at the University of North Carolina, I was given the great opportunity to work with an outstanding research group led by Joaquín Drut. Little did I know that this marked the beginning of an extremely fruitful collaboration during which I peeked into the world of computational physics and quantum matter. Despite his dense schedule, Joaquín took the time to meet with me on a daily basis, introduce me to the field (and the coffee machine) and agreed to supervise this thesis. Even when I was back in Vienna he was available in real-time, answering all of the countless questions I confronted him with. I am truly grateful for this experience and the opportunities it opened for me.
I also owe special thanks to Jay Porter, without whom the completion of this work would not have been possible. Many discussions and work-sessions in Chapel Hill as well as late-night Skype conferences across the pond have not only been productive but also a lot of fun. I am very much looking forward to continuing the work and coming back to North Carolina in the summer.
I am greatly indebted to Alessandro Toschi, who agreed to co-supervise this thesis at TU Wien. I learned a lot from our meetings and his corrections - he is responsible that this thesis became readable in the end. Thanks for taking the time despite your heavy workload, I hope it was not too stressful.
Besides the opportunity to study and work in an excellent scientific environment, I had the pleasure to meet and spend my time with many important people in my life without whom my life in Vienna would have never been the same. It has been an amazing time in a great city with people I will miss wherever I am. But for now it is time to go and to explore - not only physics, but also the world.

Contents

Chapter 1

Introduction & general formalism

> *In eighteenth-century Newtonian mechanics, the three-body problem was insoluble. With the birth of general relativity around 1910 and quantum electrodynamics in 1930, the two- and one-body problems became insoluble. And within modern quantum field theory, the problem of zero bodies (vacuum) is insoluble. So, if we are out after exact solutions, no bodies at all is already too many!*
>
> Gerald E. Brown, [1].

Whenever we set out to explore the physics of real world phenomena, we encounter the many-body problem. It is inherent to any system that is composed by a large number of interacting particles. For example, electrons in a solid are repelled by each other via the Coulomb force, thus their motion can strongly depend on the motion of the other electrons in the system. Another example is the hadronization, that is the process of the formation of composite particles (hadrons) from quarks and gluons. Moreover, hadrons can form bound states (nuclei) by interacting through the residual strong-force, constituting another non-trivial few-body problem. Last but not least, we mention the experimental progress on cold atomic gases, featuring subtle many-body effects such as Bose-Einstein condensation, superfluidity and transitions to Mott insulating states.
Evidently, the many-body problem is a central challenge on the way to understand the rich variety of effects observed in nature and experiments. The quite pessimistic initial quote from G.E. Brown captures the "problematic" aspect very well, stating that at the present time no method is available to describe many interacting particles exactly. Therefore, one is bound to find approximate approaches in order to calculate physical quantities for a given system.
Naturally, the easiest "approximation" is to ignore the interaction between particles and study the dynamics of the system, as if they moved freely. The neglection of electron-electron interaction, for instance, has led to the *Drude model*, which was proposed by P. Drude [2] to explain transport properties in metals. Surprisingly, in spite of the crude theoretical description, some of the predictions made by this model are in very good agreement with experiments. However, it is not always a good approximation to neglect the interaction between particles and therefore further analysis, including the correlation between particles, has to be done.

A way to account for the effect of particle interaction on physical quantities, is to consider it as a perturbation to the noninteracting system. One may introduce a *perturbation series* in an arbitrary but small parameter, quantifying the discrepancy between the exactly solvable model and the interacting one. Whenever the perturbative series converges once can try to expand it up to the desired accuracy and hence, obtain results for any quantity of interest. Although perturbative methods have been very successful to describe many-body physics, the approach is only applicable in the weakly interacting regime, where the screened Coloumb interaction modifies the behaviour of the system only in a controlled way. This is the case for Fermi liquid metallic systems, whose low energy properties are given by a renormalization of those of noninteracting electrons. These renormalized properties can be captured - to a large extent - by perturbation theory. However, materials with partly filled d- or f-orbitals, for example, are subject to strong correlations between electrons and therefore require a more sophisticated treatment.
Another way to reduce the complexity of the many-body problem is to rewrite it as a one-body problem in an effective *molecular field*, generated by the surrounding constituents of the system. The effective potential, in which the remaining single particle is embedded, can be computed in several ways and methods based on this technique are categorized as *mean-field* approaches. Beyond the pure mean-field theory a very successful aproach is the *density functional theory (DFT)* [3, 4], which describes physical systems as a functional of the local electronic density. The density is not assumed to be uniform and needs to be determined as a function of the spatial coordinates in order to express the corresponding terms of the Hamiltonian. Thus, the problem of solving a differential equation for $3N$ degrees of freedom is reduced to an easier one, depending only on three spatial coordinates. This approach has been the workhorse of solid-state physics for a long time and is extremely successful in describing most materials. Effects originating from strong electronic correlations, however, are still elusive within these methods due to the approximations made for the DFT functionals.
A great improvement in the characterization of strongly correlated materials was achieved by means of *dynamical mean-field theory (DMFT)* [5,6]. The approximation made within this method is to assume that the *self-energy* is a purely local quantity i.e. momentum-independent, which is exact in the limit of infinite dimensions [7]. This problem is then mapped to a so-called *impurity problem*, which can be solved by various numerical approaches. Despite the complete neglection of non-local correlations, DMFT has been applied to many materials with great success, for instance, in describing the *Mott metal-insulator transition* [8, 9].
The great variety and success of the discussed methods might suggest that mean-field approaches are the solution so long sought for. In the present work, however, we want to investigate the behaviour of strongly coupled fermions in reduced dimensions, where spatial fluctuations beyond mean-field become increasingly important. Although theoretical studies have been conducted in the early days of many-body theory, the difficulty of their experimental realization somehow limited their impact. Only when it became possible to manipulate cold atomic gases in an effective and controllable way, the theoretical exploration of low-dimensional systems started to gain attention again. Roughly twenty years ago, it became possible to prepare atomic gases at low enough temperatures, such that it is possible to observe *Bose-Einstein condensation (BEC)* [10–12]. These first advances stimulated an enormous amount of further experimental progress within the field of *ultra-*

cold quantum gases, which finally led to the realization of quasi-one-dimensional configurations in highly elongated traps as well as quasi-two-dimensional systems in pancake-shaped potentials. The observation of superfluidity in these configurations stiumlated heavy numerical calculations, in order to understand the pairing-mechanism involved in the process. Very recent studies especially focus on two-dimensional configurations, since it is believed that high-temperature unconventional superconductivity is a many-body effect triggered by the reduced dimensionality.
It is the enhanced influence of thermal and quantum fluctuations, which greatly limits the accuracy of mean-field approaches in one and two spatial dimensions. Therefore, alternative methods to describe the physics of these configurations have to be devised. Indeed, several one-dimensional models can even be treated in an exact fashion, although heavy mathematical analysis is often required. Among the exactly solvable models, we find the *1D Hubbard model* [13], which becomes intractable in higher dimensions. Unfortunately, this is not an exception. In fact, no two-dimensional many-body model is generally treatable analytically (with the exception of the famous *2D Ising model* solved by L. Onsager [14]), which limits the theoretical study of strongly correlated fermionic systems to numerical calculations away from mean-field approaches.
In this work, we investigate many-body physics at zero temperature by applying a *Quantum Monte Carlo (QMC)* method to fermionic systems on a spacetime lattice. While we should recall that not every QMC calculation is performed without further approximation we want to emphasize here that the specific approach chosen in this work is in priciple exact, up to stochasic uncertainties, reducible by improved statistics of the calculations.

1.1 Fermionic systems & the lattice

Systems consisting of large numbers of fermions, commonly referred to as *Fermi gases*, are a frequently observed phenomenon in nature. In the thermal equilibrium, their energy distribution is dictated by the *Pauli exclusion principle* which is a manifestation of *Fermi-Dirac statistics*. Pauli states that, unlike bosons, two fermions cannot occupy the same quantum state. This implies that even at zero temperature, i.e. the ground-state, some fermions are in energetically higher states than others. Therefore, in contrary to a classical ideal gas, a residual finite pressure remains in such a quantum gas at $T = 0$. This explains, for instance, the stability of neutron stars against the gravitational pull of its mass.
In this work we explore essential properties of the ground-state of interacting Fermi gases. Especially we focus on dilute Fermi systems characterized by a low particle-density. Approriate models can be chosen, such that the constraint

$$r_0 \ll k_{\mathrm{F}}^{-1} \tag{1.1}$$

is fulfilled, where r_0 defines the effective range of the interparticle potential and k_{F} denotes the *Fermi wavevector*, which is a measure for the density of the system. In this case, where the interparticle spacing is much larger than the interaction range, three- and higher-body scattering effects may be neglected. This allows us to accurately model such a gas of fermions by a small number of parameters describing the physics of two-body

collisions with *s-wave scattering*. It can be shown, in fact, that the dynamics of such systems does not depend on the exact form of the interaction as long the above constraint is not violated. The interaction between fermions in this regime is thus fully determined by the associated *s-wave scattering length* a_S and, together with the Fermi wavevector, it is the only physical parameter entering the calculation in homogenuous systems: The physics in homogenuous dilute Fermi gases is therefore completely described by the dimensionless quantity $(k_\mathrm{F} a_\mathrm{S})^{-1}$.
Such systems have been the target of many theoretical studies in recent years, ranging from one to three spatial dimensions across many interaction strengths and system sizes. In most cases however, the calculations have been performed in the so-called *thermodynamic limit (TL)*, which is achieved by taking the particle number $N \to \infty$ and the volume $V \to \infty$ at a constant particle density $n = N/V$. While these calculations provide an important connection to macroscopic observables in classical statistical mechanics, it is often interesting to investigate few-body effects, for example in light nuclei, consisting of a small number of nucleons. Furthermore, within a technique called the *virial expansion* [15] the behaviour of many-body systems can be linked under certain conditions to the correspoding few-body physics. Specifically, it has been shown that two-component Fermi gases can effectively be expressed by solutions of the two- and three-body problem, at least above a certain cutoff temperature [16, 17]. By approaching the ground-state, however, where the Fermi gas becomes increasingly degenerate, this technique does not yield accurate results any more and higher-order contributions are needed to explain the physics.
These considerations explain why the few-body regime of strongly interacting fermions is very interesting to study. We chose to tackle this problem via QMC-methods, as introduced in the next chapter. We work in the canonical ensemble with the temperature fixed to $T = 0$, whereas the particle content and the volume of the system are varied to characterize the crossover from few to many particles. The Hamiltonian for the systems in d dimensions reads as

$$\hat{H} = \int d^d x \left(- \sum_{s=\uparrow,\downarrow} \hat{\psi}_s^\dagger(\vec{x}) \frac{\hbar^2 \nabla^2}{2m} \hat{\psi}_s(\vec{x}) + g\, \hat{n}_\uparrow(\vec{x}) \hat{n}_\downarrow(\vec{x}) \right), \tag{1.2}$$

where $\hat{\psi}_s^\dagger(\vec{x})$ and $\hat{\psi}_s(\vec{x})$ are fermionic creation- and anihilation operators, respectively. Further, the density-operator $\hat{n}_s$ is defined by $\hat{n}_s \equiv \hat{\psi}_s^\dagger(\vec{x}) \hat{\psi}_s(\vec{x})$ and m denotes the mass of the particles.
It is pointed out earlier, that we perform our calculations on a spatial lattice. Therefore, we rewrite the integral in the above expression into a sum over all lattice sites i:

$$\hat{H} = \ell^d \sum_i \left(- \sum_{s=\uparrow,\downarrow} \hat{\psi}_{s,i}^\dagger \frac{\hbar^2 \nabla^2}{2m} \hat{\psi}_{s,i} + g\, \hat{n}_{\uparrow,i} \hat{n}_{\downarrow,i} \right), \tag{1.3}$$

where the spatial dependence of the occuring operator is denoted by the subscript i and the factor ℓ^d denotes the volume element originating from the lattice spacing ℓ.
Specifically, we place the system on a lattice with sides L, corresponding to a linear grid in one dimension and a square lattice in two dimensions. Thus, the reciprocal lattice, i.e. momentum space, is also discrete with a lattice spacing of $\hbar\, 2\pi/L$. Therefore, two

momentum cutoffs are introduced at low and high momenta, respectively. The former is called *infrared (IR) cutoff* and originates from the finite size of the lattice

$$\hbar\Lambda_0 = \hbar\frac{2\pi}{L}, \tag{1.4}$$

while the latter *ultraviolet (UV) cutoff* is a consequence of the lattice spacing

$$\hbar k_{\mathrm{c}} = \hbar\frac{\pi}{\ell}. \tag{1.5}$$

The kinetic energy term $\hat{T}$ in Eq. (1.3) may now be written in momentum space, as

$$\hat{T} = \ell^{-d}\sum_{k}\sum_{s=\uparrow,\downarrow}\frac{\hbar^2k^2}{2m}\hat{n}_{s,k}, \tag{1.6}$$

where $\hat{n}_{s,k}$ denotes the density-operator in momentum space and the sum is over all discrete momenta k. Hereafter, we will omit any factor of $\ell^{\pm d}$, corresponding to the specific choice of units $\ell = 1$.
Evidently, discretization errors affect any discrete lattice calculation. Therefore, the IR-cutoff needs to be controlled by the choice of a sufficiently small lattice spacing while the the UV-cutoff sets a lower bound for the size of the grid. The latter effect can be further mitigated by the use of a quadratic dispersion relation in momentum space

$$\epsilon_k = \frac{\hbar^2k^2}{2m}, \tag{1.7}$$

which is defined for momenta smaller than the UV-cutoff. This distinguishes our model from the *Hubbard model*, where typically a discrete derivative in real space is used, leading to a dispersion law of the form

$$\epsilon_k \approx \sum_{i=1}^{d}\cos(k_i\ell) \tag{1.8}$$

The drawback of the "exact" dispersion relation in Eq. (1.7) is the necessity to switch between real and momentum space via *fast Fourier tranform (FFT)*.
This discussion about the calculation on a lattice merely covers the basic aspects one needs to consider. Of course, effects caused by discretizing the calculation need to be extensively studied. A detailed discussion of the so-called *discrete variable representation (DVR)*, which represents the basis of our lattice approach, as well as associated discretization errors can be found in Refs. [18,19]. Furthermore, an overview of our method in three dimensions is provided in Ref. [20].

1.2 Partition functions & observables

In order to characterize the zero temperature behaviour of a system we need to compute expectation values of observables. In a thermodynamically stable many-body system

these expectation values are defined as

$$\langle \mathcal{O} \rangle = \langle \Omega | \, \hat{\mathcal{O}} \, | \Omega \rangle \, . \tag{1.9}$$

Here, $|\Omega\rangle$ denotes the ground-state wavefunction, which is not a-priori known for interacting systems. One way to obtain $|\Omega\rangle$ is to assume an inital state $|\Omega_o\rangle$, called a *trial wavefunction*, and project to the true ground-state of the system:

$$|\Omega\rangle = \lim_{\beta \to \infty} \hat{U}(\beta, 0) \, |\Omega_0\rangle, \tag{1.10}$$

with the definition of the imaginary time evolution operator $\hat{U}$

$$\hat{U}(\tau', \tau) \equiv e^{-(\tau' - \tau)\hat{H}}. \tag{1.11}$$

The convergence to the ground-state is guaranteed as long as the initial guess state $|\Omega_0\rangle$ has a nonvanishing projection to $|\Omega\rangle$. In this work, we take the trial wavefunction to be of the form of a *Slater determinant* in order to account for the antisymmetric nature of the fermion wavefunction. The Slater determinant is constructed from single-particle orbitals $\{\phi_k\}$, which in the case of periodic boundary conditions correspond to plane waves with momentum k. We note that this is not the only possible trial wavefunction and in fact, faster convergence can be achieved for some coupling strengths with an improved choice of the guess state, as discussed in the following chapter.
The expectation value of an arbitrary operator at finite imaginary time β can be written as

$$\mathcal{O}_\beta \equiv \frac{\langle \Omega_0 | \, \hat{U}(\beta, \beta/2) \hat{\mathcal{O}} \hat{U}(\beta/2, 0) \, | \Omega_0 \rangle}{\langle \Omega_0 | \, \hat{U}(\beta, 0) \, | \Omega_0 \rangle}, \tag{1.12}$$

and it converges to the ground-state expectation value in the limit of infinite β:

$$\langle \mathcal{O} \rangle = \lim_{\beta \to \infty} \mathcal{O}_\beta. \tag{1.13}$$

The denominator in Eq. (1.12) defines the *partition Function*

$$\mathcal{Z} \equiv \langle \Omega_0 | \, \hat{U}(\beta, 0) \, | \Omega_0 \rangle \, , \tag{1.14}$$

which we can use to obtain observables through insertion of a source term. Therefore, we rewrite the Hamiltonian to

$$\hat{H} \to \hat{H} + \eta \mathcal{O}, \tag{1.15}$$

where η is the coupling strength for an arbitrary operator $\hat{\mathcal{O}}$ of our system. To obtain the expectation value, we simply take the derivative at vanishing coupling and normalize with $\mathcal{Z}$:

$$\langle \mathcal{O} \rangle = \frac{1}{\mathcal{Z}} \frac{\partial \mathcal{Z}}{\partial \eta} \bigg|_{\eta=0} = \frac{\partial \ln \mathcal{Z}}{\partial \eta} \bigg|_{\eta=0}. \tag{1.16}$$

Specifically for the ground-state energy, we can write

$$E \equiv \langle H \rangle = -\frac{\partial \ln \mathcal{Z}}{\partial \beta}. \tag{1.17}$$

So far, we have discussed the general formalism to obtain any observable of interest. The remaining problem is the actual evaluation of these expresseion which boils down to the determination of the partition function. From Eq. 1.2, we identify the kinetic energy as

$$\hat{T} = -\sum_i \sum_{s=\uparrow,\downarrow} \hat{\psi}^\dagger_{s,i} \frac{\hbar^2 \nabla^2}{2m} \hat{\psi}_{s,i} \tag{1.18}$$

and the potential energy term as

$$\hat{V} = \sum_i \hat{n}_{\uparrow,i} \hat{n}_{\downarrow,i}. \tag{1.19}$$

It is obvious that the former is a one-body operator which is diagonal in momentum space. The potential energy is represented by a two-body operator, which marks a difficulty in our calculation, since $\hat{V}$ is not trivially diagonalizable in any basis. To deal with this instance we introcude the *auxiliary field quantum Monte Carlo (AFQMC)* formalism, which is described in Chap. 2.

1.3 Density matrices & momentum distribution

To fully describe a many-body system it is essential to study the correlation between particles at different spatial coordinates. In this work we focus on density matrices at equal imaginary times as well as the associated momentum distribution. A discussion on general properties of density matrices is omitted at this point, instead it is referred to Ref. [21] for a thorough introduction.
Our main observable of interest is the one-body density matrix, defined as

$$\rho_1(\vec{x}, \vec{x}') \equiv \langle \psi^\dagger_s(\vec{x}) \psi_s(\vec{x}') \rangle \tag{1.20}$$

It can be interpreted as the anihilation of a particle at the spatial coordinate $\vec{x}'$ and an simultanuous insertion of an identical particle at $\vec{x}$. Because we limit ourselves to the study of unpolarized systems, i.e. an equal number of fermions in every spin-flavour, the density matrices for different species coincide:

$$\langle \psi^\dagger_\uparrow(\vec{x}) \psi_\uparrow(\vec{x}') \rangle = \langle \psi^\dagger_\downarrow(\vec{x}) \psi_\downarrow(\vec{x}') \rangle. \tag{1.21}$$

To compute the above expectation value we can introduce a source term according to Eq. (1.15) and write

$$\langle \psi^\dagger_s(\vec{x}) \psi_s(\vec{x}') \rangle = \frac{\partial}{\partial \eta} \langle \Omega | e^{\eta \psi^\dagger_s(\vec{x}) \psi_s(\vec{x}')} | \Omega \rangle \Big|_{\eta=0}. \tag{1.22}$$

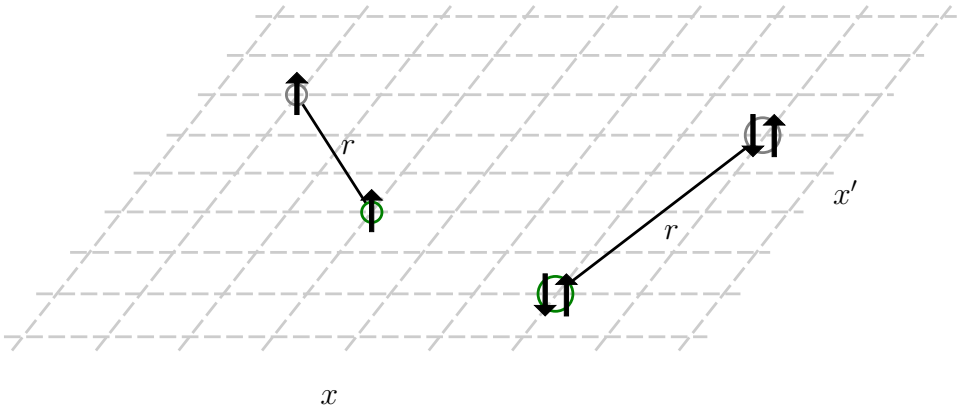

Figure 1.1: Representation of spatial one-body correlations (left) and on-site two-body correlations (right).

This form is used in the next section to derive a suitable expression for our QMC approach. Further, the one-body density matrix is connected to the momentum distribution via

$$n_k = \int d^d x \; d^d x' \; \rho_1(\vec{x}, \vec{x}') e^{ik(x-x')}, \tag{1.23}$$

where d corresponds to the dimension. Additionally, we compute the zero-size pair density matrix, defined as

$$\rho_2(\vec{x}, \vec{x}') \equiv \langle \psi_\uparrow^\dagger(\vec{x}) \psi_\uparrow(\vec{x}') \psi_\downarrow^\dagger(\vec{x}) \psi_\downarrow(\vec{x}') \rangle, \tag{1.24}$$

which encodes information about closely bound pairs consisting of two particles of opposite spin on the same lattice site. Similarly to the one-body density matrix, we can imagine a simultanous anihilation and creation of a fermionic pair at $\vec{x}'$ and $\vec{x}$, respectively. Such correlations are schematically depicted in Fig. 1.1.

1.4 The contact parameter

The physics of dilute Fermi gases with short range interactions can be described by universal relations, since it is largely determined by the s-wave scattering length. The first derivation of such relations was done by Shina Tan in a series of papers [22–24] roughly a decade ago and are known as the *Tan-relations*. The quantity occurring in all of these relations is called the contact parameter and constitues a central property of such systems. The contact can be interpreted as a measure of the number of fermion pairs of different spin which are separated by a small distance and therefore provides information about the short-range behaviour of the system.
To study its behaviour, one usually works with the *contact density* $\mathcal{C}$, defined as

$$C = \int d^d x \; \mathcal{C}(\vec{x}), \tag{1.25}$$

which is an intensive quantity and typically computed in the literature. We will exploit two different relations to extract values for the contact. Firstly, we consider the large momentum decay of the momentum distribution, which is connected to the contact via

$$\lim_{\vec{k}\to\infty} n_k = \frac{C}{\vec{k}^4}, \tag{1.26}$$

and is valid for both spin species, as shown by Tan. Therefore, we need to compute the momentum distribution and perform a fit to the tail of the distribution, as shown in chapters 3 and 4 for 1D and 2D systems, respectively. Secondly, we use an adiabatic relation which connects the contact and the change of the total energy of the system with respect to the inverse scattering length:

$$C \propto \frac{\partial E}{\partial a^{-1}}. \tag{1.27}$$

This quantity is connected to the particle interaction at constant particle number via the *Feynman-Hellman relation*

$$\frac{\partial E}{\partial g} = \langle \hat{V} \rangle_{\mathrm{N}}, \tag{1.28}$$

where the bare-coupling g depends on the s-wave scattering length a_0 from Eq. 1.27. We can exploit Eq. 1.28 as a second way to extract values for the contact.
The above relations show the importance of the contact parameter. Further euqations containing the contact involve a pressure relation, virial theorems and C also connected to inelastic two-body losses. An extensive review of the contact and further Tan-relations can be found in Ref. [25].

Chapter 2

Stochastic integration

In the introduction, we have discussed a way to extract observables from the partition functions of unpolarized Fermi gases at zero temperature, as shown in Eq. (1.16). We are, however, still confronted with the task of evaluating these expressions, which is the challenging part of this work. Specifically, in order to be able to diagonalize the interaction operator $\hat{V}$ we discretize imaginary time and perform a Hubbard-Stratonovich decomposition of the interaction, following the standard route of auxiliary-field quantum Monte Carlo (AFQMC) approaches. The price we have to pay is the occurence of high-dimensional path integrals over the introduced auxiliary fields. As these integrals cannot be solved analytically, this limits our possibilities to a stochastic approach. In this section we will show methods to solve such integrals as well as techniques to improve the quality of the estimates.

2.1 Basic ideas of Monte Carlo integration

In the previous chapter, we have shown how to obtain observables by taking expectation values using the partition function in a specific way. Expectation values are a statistical concept and take the generic form:

$$\langle A \rangle = \frac{\int_{\mathcal{D}} d\vec{x}\; A(\vec{x}) p(\vec{x})}{\int_{\mathcal{D}} d\vec{x}\; p(\vec{x})}. \tag{2.1}$$

Here, the *probability distribution function* $p(x)$ has to be non-negative on the integration domain $\mathcal{D}$ but not necessarily normalized via $\int_{\mathcal{D}} d\vec{x}\; p(x) = 1$. The integration variable $\vec{x}$ is written in vector notation to indicate the validity for any dimension. In the following, however, we will limit ourselves to the one-dimensional notation.
One is able to evaluate such integrals for known probability distributions, e.g. a Gaussian, analytically. For arbitrary or even unknown distributions one is in general not able to solve the above expression exactly and is therefore limited to a numerical evaluation. A straightforward approach would be to slice the integration domain into segments of length Δx_i, calculate the area of these slices by $A_i = f(x_i)\Delta x_i$ and sum them in order to get a value for the integral up to discretization errors. Although this simple *deterministic* strategy can be refined in many ways a serious dimensionality problem remains: In order to integrate over a d-dimensional domain one needs to discretize every dimension separately, leading to heavy computational effort since the total number of integration points

grows exponentially in d. Thus, for high-dimensional integrals such as the path integrals emerging from the AFQMC approach, one still needs to find an appropriate way to obtain a solution. One possibility is to estimate the value of the integral via a stochastic approach such as Monte Carlo integration, which typically become the preferred method for a number of dimensions greater than 5.
There are many strategies and algorithms how this can be done for a vast variety of models. Therefore, we will only present here an introduction to the specific approach of this work. A very thorough treatment can be found in Ref. [26].

2.1.1 Simple sampling strategies

Let us assume that we want to stochastically estimate an integral of the form (2.1). A straightforward way, termed the *crude method*, is to sample N randomly selected points x_i of the integration domain and calculate the weighted mean by

$$\langle A \rangle_{\text{MC}} = \frac{\frac{V}{N} \sum_i^N A(x_i) p(x_i)}{\frac{V}{N} \sum_i^N p(x_i)}, \tag{2.2}$$

which will play the part of the *Monte Carlo estimate* $\langle A \rangle_{\text{MC}}$ for now. Here, V denotes the volume of the integration domain. This estimate is connected to the real value of A via

$$\langle A \rangle = \langle A \rangle_{\text{MC}} + \mathcal{O}\left(\frac{1}{N^\alpha}\right), \tag{2.3}$$

where one still needs to specify the exponent α of N in the scaling of the uncertainty. For this, we assume a uniform probability distribution with

$$p(x) = \frac{1}{V} \tag{2.4}$$

which is trivially normalized to 1. Therefore, expression (2.2) simplifies to

$$\langle A \rangle_{\text{MC}} = \frac{1}{N} \sum_i^N A(x_i). \tag{2.5}$$

In order to get an estimate for the error, one can exploit the *central limit theorem*. In one of its many variants it can be formulated as following: For a sequence of independent and identically distributed random variables the error $\epsilon = \langle A \rangle_{\text{MC}} - \langle A \rangle$ of the estimate follows a *normal distribution* with variance σ^2_{MC}:

$$\sqrt{N}\epsilon \to N(0, \sigma^2_{\text{MC}}). \tag{2.6}$$

If we now define the variance of the Monte Carlo estimate as

$$\sigma^2_{\text{MC}} = \langle A^2 \rangle_{\text{MC}} - \langle A \rangle^2_{\text{MC}}, \tag{2.7}$$

we can identify

$$\sigma_\epsilon^2 = \frac{\sigma_{\text{MC}}^2}{N} \tag{2.8}$$

and therefore have determined the exponent from expression (2.3) to be $\alpha = \frac{1}{2}$ in the uniformly distributed case. In principle, such a calculation can be done for any given distribution it is in general not so straightforward to see and is therefore omitted at this point. We further note that this is just an estimate for the real error, since the error of the Monte Carlo estimate might not follow a Gaussian distribution due to systematic effects. Assuming that this is the case for the moment we can see the poor scaling of such a calculation: In order to incerase the accuracy by one decimal place one needs to obtain 100 times as many samples as before. Clearly, this will eventually limit the achievable precision and one needs to exploit more sophisticated strategies to achieve lower errors at a comparable number of samples. Such methods are discussed in the upcoming sections.

2.1.2 Importance sampling

A first approach to reduce the variance in Monte Carlo calculations besides increasing the statistics is to sample the random configurations in a more favorable way. To do so, we want to draw the random variables from an arbitrary distribution $g(x)$ unlike before, where we assumed the probability distribution $p(x)$ to be uniform. If $g(x)$ is chosen appropriately, we can diminish the amount of samples drawn from regions which are not significant to the value of the integral, hence the name *Importance Sampling*. Quantitatively, we need to reweight the probability distribution as:

$$\langle A \rangle = \frac{\int_{\mathcal{D}} dx A(x)p(x)}{\int_{\mathcal{D}} dx p(x)} = \langle A \rangle = \frac{\int_{\mathcal{D}} dx \frac{A(x)p(x)}{g(x)} g(x)}{\int_{\mathcal{D}} dx \frac{p(x)}{g(x)} g(x)} \tag{2.9}$$

which corresponds to the absorption of the weight $g(x)$ into the random numbers. This changes the variance, which now reads

$$\sigma_\epsilon^2 = \frac{1}{N} \sigma_{\text{MC}} \left(\frac{Ap}{g} \right) \tag{2.10}$$

where the notation $\sigma_{\text{MC}}(\frac{Ap}{g})$ indicates the dependence on the reweighted distribution. It can be shown that the optimal choice for the new probability distribution is given by

$$g(x) = \frac{|A(x)p(x)|}{\int_{\mathcal{D}} dx |A(x)p(x)|} \tag{2.11}$$

This minimum in the variance corresponds to the probability distribution that follows the functional $A(x)p(x)$ as closely as possible.
Unfortunately, this method has a major drawback in many cases: for the generation of random numbers according to a desired probabilty distribution $g(x)$, we need to know the inverse of the cumulative distribution function $G(x)$. This becomes especially problem-

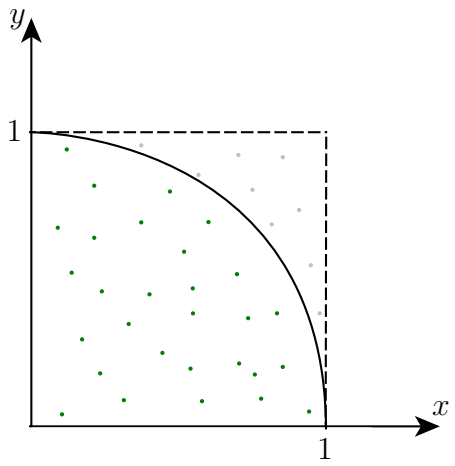

Figure 2.1: Calculation of π as an example for hit-or-miss sampling.

atic for QMC calculations, where we use the partition function $\mathcal{Z}$ as the weight. Computing $\mathcal{Z}$ and inverting it constitutes a very challenging problem and therefore would result in an equally heavy or even heavier numerical workload, if possible at all. For this reason, we need to introduce methods to overcome these difficulties, which is done in the next sections.

2.1.3 Rejection sampling

An algorithm to sample an arbitrary distribution function without having to compute the cumulative distribution is provided by *rejection sampling*. This concept is the basis of the *Metroplis algorithm* discussed below.
Assume that sampling the target distribution function $p(x)$ is very difficult. The main idea behind rejection sampling is to use a proposal distribution $g(x)$ which fulfills the constraint

$$p(x) < Mg(x) \tag{2.12}$$

and is easier to sample than $p(x)$. Here, M denotes a non-negative but finite constant. As a first step, we sample a random point x_i according to the proposal distribution. Next, we uniformly draw a value u from the interval $[0, 1]$ and accept the value if it fulfills the constraint

$$u < \frac{g(x)}{Mp(x)}, \tag{2.13}$$

i.e. we only accept values that fall below the target distribution and therefore sample according to $p(x)$.
A simple, yet very prominent example of rejection sampling is the calculation of π, as depicted in Fig. 2.1: Following the strategy described above, one counts how many of the corresponding coordinates in the xy-plane fall below the curve. This allows us to estimate

π by calculating

$$\pi \approx 4\frac{N_h}{N}, \tag{2.14}$$

where N is the total number of random coordinates and N_h counts the ones that hit the target.
This method constitutes an improvement to the previously discussed concepts, but still suffers from a dimensionality problem. To generalize our example, we now want to calculate the volume of a hyper-sphere in d-dimensions. The largest contribution to its value for large d originates from the vicinity of the surface which, when sampling uniformly along the "radius", leads to a large amount of rejects, thus an increased numerical effort.

2.1.4 Markov chains, detailed balance & ergodicity

In order to describe a stochastic process, e.g. a random walk in some configuration space $\mathcal{C}$, it is sometimes sufficient to consider only the current configuration to calculate the future state of the system. This corresponds to a loss of memory for earlier configurations and such a sequence of random variables is called a *Markov chain*. We can model such a random walk as jumps from a configuration x to a configuration x', with the transition probability $t(x \to x')$. Then the probability to find the system in the state x, when it previously was in the state x', is given by

$$p(x|x') = t(x \to x')p(x'). \tag{2.15}$$

This sequence is designed to asymptotically reach the probability distribution $p(x)$ if the detailed balance constraint is satisfied, that is

$$t(x' \to x)p(x) = t(x \to x')p(x'), \tag{2.16}$$

which corresponds to the reversibility of the chosen path. Furthermore, the principle of *ergodicity* should also be fulfilled, meaning that every state can be reached with a finite number of jumps. In other words, if the system is ergodic no region of the configuration space will be neglected. Then, the Monte Carlo average $\langle A\rangle_{\text{MC}}$ converges to the true expectation value $\langle A\rangle$ of the desired observable:

$$\lim_{N\to\infty} \langle A\rangle_{\text{MC}} \to \langle A\rangle. \tag{2.17}$$

2.1.5 Metropolis algorithm

Although a state from the configuration space $\mathcal{C}$ might have a complicated structure it is in principle straightforward to construct a random sample from scratch. Computationally, on the other hand, the creation of a single state implies many operations, accumulating to a significant computation time when the process is iterated for every new configuration. In order to keep the numerical effort at a minimum, one can exploit the properties of Markov chains and combine it with the rejection sampling strategy discussed above, which is the main idea behind the *Metropolis algorithm* [27, 28]. Starting out from a randomly generated state, one may proceed by updating the configuration, e.g. by changing the local

value of an auxiliary field introduced in Sec. 2.2, and accept it with a certain probability depending on the current state of the system.
In order to compute the value of an observable $\mathcal{O}$, again a number of N samples have to be selected according to the desired distribution function. Then we can calculate

$$\langle \mathcal{O} \rangle_{\text{MC}} = \frac{1}{N} \sum_{N} \mathcal{O}(\Sigma) \tag{2.18}$$

where Σ denotes a state from the configuration space $\mathcal{C}$. We assume that such a state collects every possible variable available in the system. The remaining problem is to produce the states Σ according to the desired probability distribution $p(\Sigma)$.
In practice, one starts out with an inital state Σ and picks out a number of M random variables, e.g. values of spatial auxiliary fields, for which the numerical value will be altered. An updated state Σ' is obtained by this updated process and the probability to accept this new configuration is given by

$$p = \min\left(1, \frac{p[\Sigma']}{p[\Sigma]}\right). \tag{2.19}$$

The above expression states that the new configuration is accepted if it is more probable than the old one or accepted with a certain probability if it is less likely. This corresponds to a random walk in configuration space where we use the intermediate steps as samples to obtain an expectation value for the desired observable. The configurations created by this procedure follow the desired probability distribution $p(\Sigma)$ in the limit of $N \to \infty$.
The benefit from this approach is that we do not have to build a new state for every sample but rather update a number of variables and use the existing structure to save computation time. Of course, one has to be very careful upon performing such random walks, since the finite number of local updates evidently limits the distance one can move in configuration space. In the limit of only one local update, in fact, it could be very hard to move away from a local minimum, i.e. ergodicity might be violated, which would result in a bias of the obtained estimate. Hence, for all calculations the choice of the sweep-size M needs to be done carefully in order to get accurate results.

2.2 Quantum Monte Carlo

After the introduction of basic concepts of Monte Carlo integration, we will now focus on the way to evaluate the expressions previously obtained in Sec. (1.2). We will, however, limit ourselves to consider the specific problem of interest in this work. For a more sophisticated treatment of lattice quantum Monte Carlo methods see Refs. [30, 31].
We start here by recalling the definition of the expectation value of an operator at finite imaginary time from Eq. (1.12):

$$\mathcal{O}_\beta = \frac{\langle \Omega_0 | \hat{U}(\beta, \beta/2) \hat{\mathcal{O}} \hat{U}(\beta/2, 0) | \Omega_0 \rangle}{\langle \Omega_0 | \hat{U}(\beta, 0) | \Omega_0 \rangle}, \tag{2.20}$$

where $|\Omega_0\rangle$ denotes the initial Slater-determinant as introduced in Sec. 1.2 and the evolution operator $\hat{U}(\tau, \tau')$ is defined as

$$\hat{U}(\tau, \tau') \equiv e^{-(\tau-\tau')\hat{H}}. \tag{2.21}$$

The Hamiltonian $\hat{H}$ of the system is given by

$$\hat{H} = \hat{T} + g\hat{V}. \tag{2.22}$$

The kinetic and interaction parts $\hat{T}$ and $\hat{V}$ of $\hat{H}$ are in general non-commuting, which makes a simultaneous diagonalization a priori impossible. There exist, however, numerous strategies in order to deal with the computation of the evolution operator $\hat{U}$ and hence, the dynamics of the system. One way to do so is to discretize the imaginary time into small slices according to a *Suzuki-Trotter-decomposition*

$$\hat{U}(\tau + \Delta\tau, \tau) = e^{-\Delta\tau\frac{\hat{T}}{2}} e^{-\Delta\tau\hat{V}} e^{-\Delta\tau\frac{\hat{T}}{2}} + \mathcal{O}(\Delta\tau^3) \tag{2.23}$$

which corresponds to an approximation of the evolution operator whose error diminishes with decreasing discretization length

$$\Delta\tau = \frac{\beta}{N_\tau}. \tag{2.24}$$

Details on the derivation of the above expression are shown in App. C. Here we simply note that methods were devised recently, which overcome the systematic effect of such a time-discretization. Such methods are often referred to as *continuous-time QMC (CTQMC)* methods, see e.g. Ref. [29]. We will, however, work with a discretized time since we utilize the *hybrid Monte Carlo (HMC)* approach which is not yet adapted for a continuous time variable.
Although we have split the Hamiltonian into the kinetic and interaction part, we still have to deal with the problem that we cannot diagonalize the two-body interaction operator $\hat{V}$. To overcome this difficulty we introduce auxiliary fields σ, which decouple the particles of different flavour:

$$e^{-\Delta\tau\hat{V}} = \int_{\mathcal{C}} \mathcal{D}\sigma(\vec{x})\; e^{-\Delta\tau\hat{V}_{\uparrow,\sigma}} e^{-\Delta\tau\hat{V}_{\downarrow,\sigma}}. \tag{2.25}$$

This is called a *Hubbard-Stratonovich transformation* and constitutes the basis of a class of methods called *auxiliary-field QMC (AFQMC)*. In the above expression, $V_{s,\sigma}$ are one-body operators which depend on the Hubbard-Stratonovich field $\sigma(x)$ and $\int_{\mathcal{C}} \mathcal{D}\sigma(\vec{x})$ is a sum over all possible configurations at a specific time-slice τ. Further, we notice that the path-integral over all possible auxiliary fields could be done in a discrete way, as a consequence of Fermi-statistics. We will, for reasons discussed below, use the continuous notation and refer to App. D for the exact expressions, as well as for further details about the decomposition of the interaction.
The above decomposition of the interaction allows us to compute the partition function and observables at the cost of evaluating the introduced path integrals. In other words: instead of solving one very complicated many-body problem, we reduce it to a large number of one-body problems in the presence of an external field. The occurring integrals

are extremely high-dimensional, since we introduce one spatial auxiliary variable per temporal lattice site. In order to evaluate these integrals, we will use the *Hybrid Monte Carlo (HMC)* algorithm which will be introduced in Sec. 2.2.2.

2.2.1 Partition function & observables

With the decomposition of the interaction introduced in the previous section, we are now able to expand the expressions for the partition function as obtained in Sec. (1.2) as

$$\mathcal{Z} \equiv \langle \Omega_0 | \, \hat{U}(\beta, 0) \, | \Omega_0 \rangle = \int_{\mathcal{C}} \mathcal{D}\sigma(\vec{x}, t) \; P[\sigma] \tag{2.26}$$

where we again used the schematic notation of the integral. We note that the integration now also covers the temporal extent of the lattice. The integrand is the probability measure defined by

$$P[\sigma] \equiv \langle \Omega_0 | \, \hat{U}_\sigma(\beta, 0) \, | \Omega_0 \rangle \tag{2.27}$$

with

$$\hat{U}_\sigma(\tau + \Delta\tau, \tau) = e^{-\Delta\tau \frac{\hat{T}}{2}} e^{-\Delta\tau \hat{V}_{\uparrow,\sigma}} e^{-\Delta\tau \hat{V}_{\downarrow,\sigma}} e^{-\Delta\tau \frac{\hat{T}}{2}}. \tag{2.28}$$

Rewriting Eq. (2.27) in terms of the single-particle wavefunctions $\{\phi_k\}$ yields

$$P[\sigma] = \left(\det \left[M_\sigma(\beta)\right]\right)^2, \tag{2.29}$$

where

$$\left[M_\sigma(\beta)\right]_{ij} \equiv \langle i | \, \hat{U}_\sigma(\beta, 0) \, | j \rangle \tag{2.30}$$

is the single-particle representation matrix of the product operator $\hat{U}_\sigma(\beta, 0)$. The square in Eq. (2.29) originiates from the fact that we consider two distinguishable but otherwise identical species of fermions. This ensures the non-negativity of the integration measure and therefore avoids an otherwise occuring sign-problem, as it will be descussed more extensively below.
In the same way, we can rewrite the expression for an arbitrary operator. Eq. (1.12) then becomes

$$\mathcal{O}_\beta = \frac{1}{\mathcal{Z}} \int_{\mathcal{C}} \mathcal{D}\sigma(\vec{x}, t) \; P[\sigma] \mathcal{O}[\sigma] \tag{2.31}$$

and we identify

$$\mathcal{O}[\sigma] = \frac{\langle \Omega_0 | \, \hat{U}_\sigma(\beta, \beta/2) \hat{\mathcal{O}} \hat{U}_\sigma(\beta/2, 0) \, | \Omega_0 \rangle}{\langle \Omega_0 | \, \hat{U}_\sigma(\beta, 0) \, | \Omega_0 \rangle} \tag{2.32}$$

as the contribution to the operator $\mathcal{O}$ for a specific value of the auxiliary field σ. As we are working at finite β, the expectation values in the true ground-state of the system is only obtained by an extrapolation to infinite imaginary time according to Eq. (1.13).

Ground-state energy

For the ground-state energy, we can differentiate the partition function with respect to β

$$E_\beta = -\frac{\partial \ln \mathcal{Z}}{\partial \beta} = -\frac{1}{\mathcal{Z}} \frac{\partial \mathcal{Z}}{\partial \beta} \tag{2.33}$$

and rewrite it in terms of the single-particle matrix representation $M_\sigma(\beta)$:

$$E_\beta = -\frac{1}{\int_\mathcal{C} \mathcal{D}\sigma \ \det\left[M_\sigma(\beta)\right]^2} \frac{\partial}{\partial \beta} \int_\mathcal{C} \mathcal{D}\sigma \ \det\left[M_\sigma(\beta)\right]^2. \tag{2.34}$$

Using the relation

$$\ln \det A = \mathrm{Tr} \ln A \tag{2.35}$$

for arbitrary matrices A and perfom the differentiation, we can further rewrite Eq. (2.34) to

$$E_\beta = -\frac{2}{\int_\mathcal{C} \mathcal{D}\sigma \ \det\left[M_\sigma(\beta)\right]^2} \int_\mathcal{C} \mathcal{D}\sigma \ \det\left[M_\sigma(\beta)\right]^2 \ \mathrm{Tr} \frac{\partial \ln M_\sigma(\beta)}{\partial \beta}. \tag{2.36}$$

Since $M_\sigma(\beta)$ depends on the auxiliary fields, which in turn depend on the time-discretization, we need to perform the differentiation in τ and get

$$E_\beta = -\frac{2}{N_\tau} \frac{1}{\int_\mathcal{C} \mathcal{D}\sigma \ \det\left[M_\sigma(\beta)\right]^2} \int_\mathcal{C} \mathcal{D}\sigma \ \det\left[M_\sigma(\beta)\right]^2 \ \mathrm{Tr} \left[M_\sigma^{-1}(\beta) \frac{\partial M_\sigma(\beta)}{\partial \tau} \right], \tag{2.37}$$

Finally, we can absorb the prefactor $1/\mathcal{Z}$ into the probability measure and obtain a normalized estimator for the ground-state energy:

$$E_\beta = -\frac{2}{N_\tau} \int_\mathcal{C} \mathcal{D}\sigma \ \tilde{P}[\sigma] \ \mathrm{Tr} \left[M_\sigma^{-1}(\beta) \frac{\partial M_\sigma(\beta)}{\partial \tau} \right] \tag{2.38}$$

with

$$\tilde{P}[\sigma] = \frac{\det\left[M_\sigma(\beta)\right]^2}{\int_\mathcal{C} \mathcal{D}\sigma \ \det\left[M_\sigma(\beta)\right]^2}. \tag{2.39}$$

The form of this expression allows us to sample the ground-state energy stochastically. Additionally, it is straightforward to see that the differential operator in Eq. (2.34) separates the contributions from the kinetic and the interaction part of the Hamiltonian. Therefore, we obtain expectation values not only for the total energy of the system, but also separately for its constituents. This allows us to calculate further quantites, e.g. the contact parameter, as introduced in Sec 1.4.

Density matrices

We will now compute the estimator for the one-particle density matrix, closely following the derivation given in Ref. [21]. The one-body density matrix for a specific auxiliary

field configuration is given by

$$\rho_{1,\sigma}(x,x') = \langle \psi^\dagger(x)\psi(x')\rangle_\sigma. \tag{2.40}$$

Here and in the following, the spin-index was omitted for a more compact notation. To obtain the observable, we again need to perform a path integral over all auxiliary field configurations σ:

$$\rho_1(x,x') = \int_{\mathcal{C}} \mathcal{D}\sigma\, P[\sigma]\, \rho_{1,\sigma}(x,x'). \tag{2.41}$$

Rewriting Eq. 2.40 with a source term and taking the derivative according to Eq. 1.16 yields

$$\rho_{1,\sigma}(x,x') = \frac{\partial}{\partial\eta} \ln \langle\Omega_0|\, \hat{U}_\sigma(\beta,\beta/2)\, e^{\eta\psi^\dagger A(x,x')\psi}\, \hat{U}_\sigma(\beta/2,0)\, |\Omega_0\rangle \,\Big|_{\eta=0} \tag{2.42}$$

where $A(x,x')$ can be written as $|x\rangle\langle x'|$. Now we can exploit some properties of Slater determinants which are derived in Ref. [21]. Since our Hamiltonian was rewritten such that only single-partilce operators occur, we are able to use the fact that the application of an exponential of a single-particle operator on a Slater determinant again results in a Slater determinant. Further, the contraction of two Slater determinants can be written as a determinant of the evolved waves

$$\phi_{1,\sigma}(\beta) \equiv \prod_{i=1}^{N/2} \phi_{\sigma,i}(\beta) \equiv \prod_{i=1}^{N/2} \hat{U}_\sigma(\beta)\, |i\rangle \tag{2.43}$$

where $|i\rangle$ is a single-particle state. Applying these properties gives

$$\rho_{1,\sigma}(x,x') = \frac{\partial}{\partial\eta} \ln\det\left[\phi^\dagger_\sigma(\beta/2)\, e^{\eta A(x,x')}\, \phi_\sigma(\beta/2)\right] \Big|_{\eta=0}. \tag{2.44}$$

Now we can again rewrite this expression via Eq. 2.35

$$\rho_{1,\sigma}(x,x') = \frac{\partial}{\partial\eta} \mathrm{Tr} \ln\left[\phi^\dagger_\sigma(\beta/2)\, e^{\eta A(x,x')}\, \phi_\sigma(\beta/2)\right] \Big|_{\eta=0}. \tag{2.45}$$

Applying the differential operator yields

$$\rho_{1,\sigma}(x,x') = \mathrm{Tr}\Big[M^{-1}_\sigma(\beta)\, \phi^\dagger_\sigma(\beta/2)\, A(x,x')\, \phi_\sigma(\beta/2)\Big] \tag{2.46}$$

and finally we use the cyclic property of the trace to write

$$\rho_{1,\sigma}(x,x') = \sum_{i,j=1}^{N/2} \phi^*_{\sigma,i}(\beta/2,x)\, [M^{-1}_\sigma(\beta)]_{ij}\, \phi_{\sigma,j}(\beta/2,x'), \tag{2.47}$$

whith the definition

$$\phi_{\sigma,i}(\beta,x) \equiv \langle x|\, \hat{U}_\sigma(\beta)\, |i\rangle\,. \tag{2.48}$$

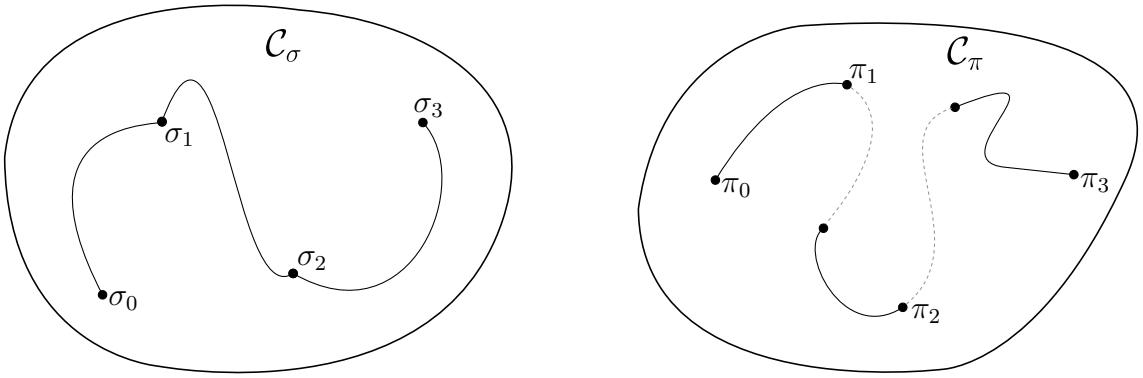

Figure 2.2: Schematic movement in the configuration spaces $\mathcal{C}_\sigma$ and $\mathcal{C}_\pi$ as performed by the HMC-algorithm. The left panel shows the propagation of the Hubbard-Stratonovich fields σ while on the right the evolution of the introduced momentum field π is depicted. Solid lines represent on-shell propagation from $\sigma_n(\pi_n)$ at time t_n to $\sigma_{n+1}(\pi_{n+1})$ at t_{n+1}, whereas the dashed lines indicate a discontinuous jump between energy shells. The latter only occur in the momentum fields, due to resampling at every new configuration of σ.

Eq. 2.47 can now be used to sample the one-body density matrix for particles with equal spin. Since we performed a HS-transformation, the operators for different spin-species decouple and we can simply write the zero-size pair-correlation as a product of the corresponding single-particle density matrices:

$$\rho_{2,\sigma}(x,x') = \int_{\mathcal{C}} \mathcal{D}\sigma\, P[\sigma]\, \rho_{1,\sigma,\uparrow}(x,x')\rho_{1,\sigma,\downarrow}(x,x') = \int_{\mathcal{C}} \mathcal{D}\sigma\, P[\sigma]\, \left[\rho_{1,\sigma}(x,x')\right]^2. \quad (2.49)$$

2.2.2 Hybrid Monte Carlo

As discussed earlier, the computationally expensive creation of many random samples from the configuration state is avoided by introducing the Metropolis algorithm. For a very complicated structure of the phase-space, however, the efficiency of such methods, often referred to as *Deterministic Monte Carlo (DMC)*, suffers from a very low acceptance rate. The obvious solution is to reduce the sweep-size, i.e. to reduce the number of random local updates. While this raises the acceptance rate, the correlation between subsequent samples increases, leading to a bias in the computed expectation values. The competition of sweep-size reduction at a sufficient decorrelation between the samples have the consequence of a minimal computational cost for a useful configuration, limiting the efficiency of such methods.
A way to reduce the cost for a full sweep is given by the *Hybrid Monte Carlo (HMC)* algorithm, introduced in Ref. [32]. Unlike in DMC, where updates of states are done locally, in HMC an update is done globally, affecting the entire configuration at each point on the spacetime lattice. The resulting states are then accepted or rejected according to the Metropolis algorithm. The global update is done by introducing *molecular dynamics (MD)* as shown in the following.
As a first step towards the HMC algorithm, we expand the probability measure from Eq.

(2.26) with a Gaussian-distributed momentum field π:

$$P[\sigma, \pi] = e^{-\sum_{n,\tau} \frac{\pi_{n,\tau}^2}{2}} P[\sigma] \tag{2.50}$$

The path-integral then becomes

$$\mathcal{Z} = \int \mathcal{D}\sigma \mathcal{D}\pi \; P[\sigma, \pi]. \tag{2.51}$$

The sum in Eq. (2.50) is over all spacetime lattice sites and therefore traces out any degree of freedom of this fictitious field. The resulting multiplicative factor is constant, thus, does not change the dynamics of the problem. Hence, the probability measures defined in Eq. (2.27) and Eq. (2.50) are physically equivalent.
Thus far, it might seem counter-intuitive to expand the integration measure by further degrees of freedom, which makes sampling even more complicated. The advantage of this, however, can be understood by inspecting the definition of a corresponding Hamiltonian

$$\mathcal{H}_{\text{MD}} = \sum_{n,\tau} \frac{\pi_{n,\tau}^2}{2} - \ln P[\sigma] \equiv \sum_{n,\tau} \frac{\pi_{n,\tau}^2}{2} + S_{\text{eff}}[\sigma], \tag{2.52}$$

where S_{eff} is an effective action. The introduced integration measure can then be written as

$$P[\sigma, \pi] = e^{-\mathcal{H}_{\text{MD}}} \tag{2.53}$$

allowing us to treat the problem with the classical equations of motion, which allow for a straightforward to integration:

$$\frac{d}{dt_{\text{MD}}} \sigma_{n,\tau} = \pi_{n,\tau} \tag{2.54a}$$

$$\frac{d}{dt_{\text{MD}}} \pi_{n,\tau} = -\frac{\delta S_{\text{eff}}[\sigma]}{\delta \sigma_{n,\tau}} \tag{2.54b}$$

The timescale t_{MD} for the MD-calculation is purely fictitious allowing us to tweak the parameters such that both accuracy and performance are optimized. For a sufficiently long trajectory in t_{MD}, a fully updated configuration is generated. Although many methods exist to integrate the above equations of motion, which are typically very accurate, there are numerical errors. For this reason we need to verify if the new, globally updated states correspond to the desired probability distribution, i.e. perform a rejection-check according to the Metropolis algorithm. The accuracy of the integrators leads to very high acceptance rates, often in the region of 99%. In order to move between energy shells, we randomize the introduced momentum-field at the begin of a new MD-evolution, corresponding to a sampling of the π-integral in Eq. (2.51). The random walk in configuration space is schematically depicted in Fig. 2.2. Additionally, a flow-diagram which contains an overview of the implemented HMC-method is provided in Fig. 2.3.

2.2.3 The negative sign problem

To conclude this chapter, we will now discuss the problem of a negative sign in the probability measure, which is inherent to QMC simulations of fermions. Part of the reason for the so-called *negative sign problem* is the *Grassmann*-nature of fermionic fields, which fulfill anticommutator relations. Unlike in the bosonic case, where the commutation of creation- and annihilation operators always yields a positive sign, the corresponding fermionic anticommutator relations produce an oscillating sign. A straightforward way to overcome this issue is to include the sign in the calculated observable ($p(x) = s(x)|p(x)|$) and then sample the absolute value of the weights:

$$\langle A\rangle_{\mathrm{MC}} = \frac{\sum_x A(x)p(x)}{\sum_x p(x)} = \frac{\sum_x A(x)|p(x)|s(x)/\sum_x |p(x)|}{\sum_x |p(x)|s(x)/\sum_x |p(x)|} \equiv \frac{\langle As\rangle_{\mathrm{MC}}}{\langle s\rangle_{\mathrm{MC}}} \tag{2.55}$$

Although reweighting enables the use of Monte Carlo methods the associated statistical error of the expectation value scales exponentially with increasing particle number due to the cancellation of the mean sign $\langle s\rangle$. This leads to an exponential increase in computation time to achieve reasonably small errors. In many models it is possible to overcome this issue by an appropriate choice of parameters, e.g. half-filled (i.e. particle-hole symmetric) Hubbard model or unpolarized Fermi gases. This, however, limits the explorable physics greatly and raises the need for a general solution for this problem which is, in fact, NP-hard [33] and therefore unlikely to be solved.
To demonstrate the sign-problem in our formalism, we write the general form of Eq. (2.29), lifting the assumption of equally populated spin-species:

$$P[\sigma] = \prod_s \det M_{\sigma,s}(\beta) \tag{2.56}$$

where the product includes all spin flavours s. As mentioned above, $P[\sigma]$ will stay positive for an even number of species with equal population and attractive interaction. For an unequal population of the spin states the matrices do not coincide and we can not simply take the square of the determinant any more. Furthermore, for repulsive interactions, the matrix contains imaginary elements, which could yield negative contributions even in the unpolarized system. In such cases the measure is not guaranteed to be non-negative and therefore Eq. 2.56 does not provide a good probability distribution. A possible extension is to introduce an imaginary imbalance followed by an analytic continuation in order to explore a larger region of the associated phase-diagram, as e.g. done in Ref. [34].

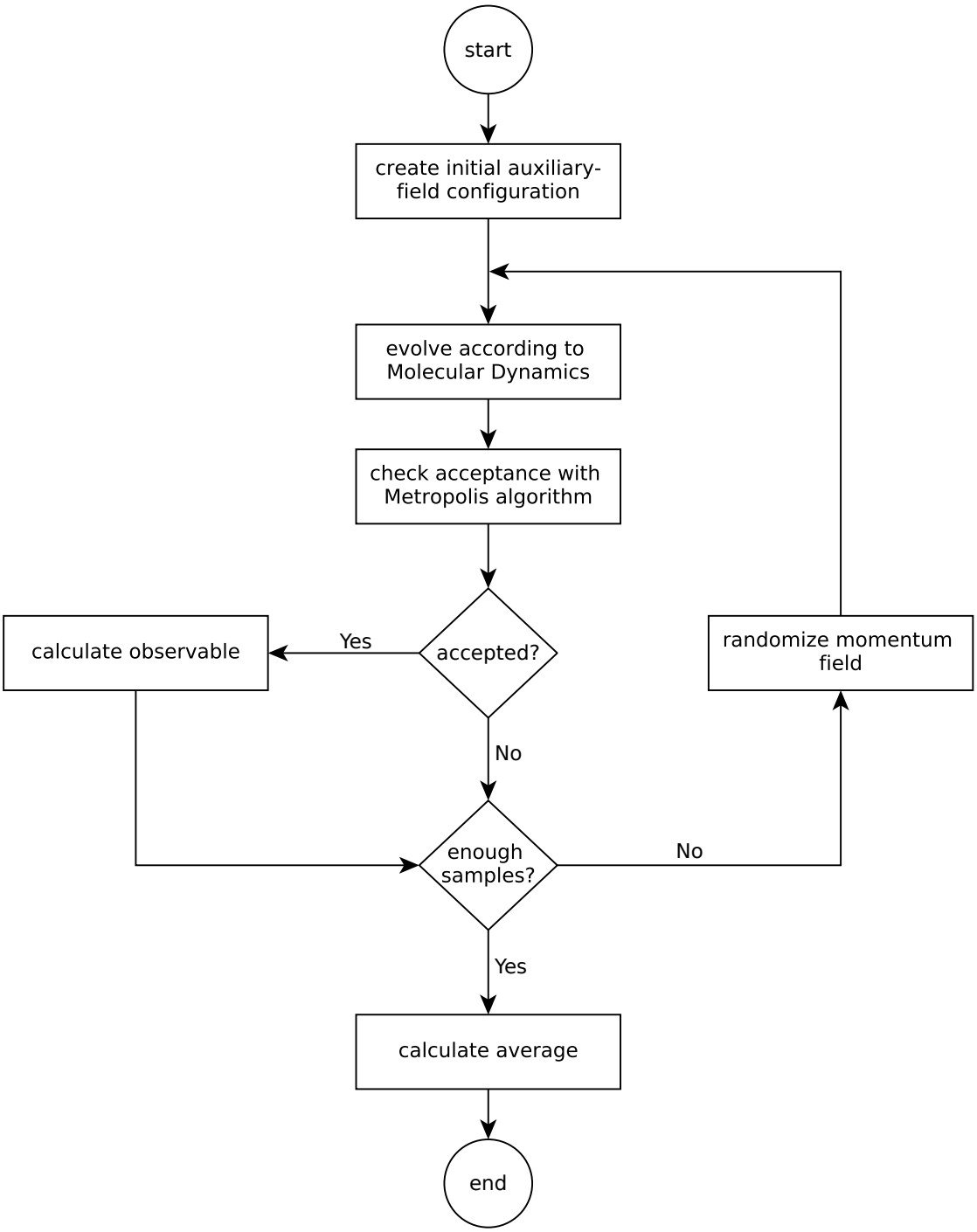

Figure 2.3: Flow Diagram of the discussed QMC method. A random field configuration is created and globally updated by means of Molecular Dynamics. If the generated intermediate step is accepted corresponding observables are calculated. This process is iterated until a sufficient number of MC-steps is reached. Finally, the MC-average is computed.

Chapter 3

The one-dimensional Fermi gas

In this section we discuss the physics of a nonrelativistic, one-dimensional (1D) Fermi gas on a lattice at zero temperature. Although the Bethe ansatz technique provides a way to solve this problem, we choose to use Monte Carlo methods to investigate this system. In fact, while the first approach is restricted to one-dimensional calculations with no external potential, the latter does not face this limitation. Moreover, the presented calculations are not only interesting for themselves, but they also provide a benchmark for subsequent studies in higher dimensions, as discussed in the next chapter.
In particular, we focus on systems represented by a one-dimensional box with periodic boundary conditions (i.e. a ring) for an equal number of spin-up and -down fermions to avoid sign problems. To characterize the response of the system, we calculate the one- and two-particle density matrices at equal imaginary times. Furthermore, we compare momentum distributions for a wide range of attractive couplings, from which we extract the contact parameter and perform a comparison to previous results, wherever possible. Finally, we will analyze systematic errors mostly originating from the finite lattice size and effective inverse temperature of the system.

As mentioned in the introduction, low dimensional systems exhibit a fundamentally different behaviour as compared to their more familiar counterparts in three dimensions. The modified behaviour becomes evident especially in 1D systems, where the Fermi surface reduces to two points located at $\pm k_F$ (see Fig. 3.1), with k_F being the Fermi momentum. Moreover, the available phase-space for 1D systems is so limited that the concept of Fermi liquids is no longer applicable due to effects like the *Peierls-instability* and *spin-charge separation*. The elementary excitations in 1D can no longer be interpreted as quasi-particles, but are rather represented by collective oscillations (i.e. density waves), which display a radically different behaviour than noninteracting, renormalized fermions (i.e. Landau quasi-particles).

Although our world is clearly three-dimensional, it is for such a fundamentally different behaviour that 1D systems are interesting to investigate. Moreover, there are important experiments and devices, where the electronic motion is effectively confined to 1D. One very prominent example is the carbon nanotube, which is believed to have many industrial applications. More importantly, there has been recent experimental progress in confining ensembles of ultracold atoms to effectively one dimension [37]. The interparticle interaction is then controlled via so-called *Feshbach-resonances* [36], resulting in the possibility to study 1D systems ranging from strongly repulsive to strongly attractive interaction.

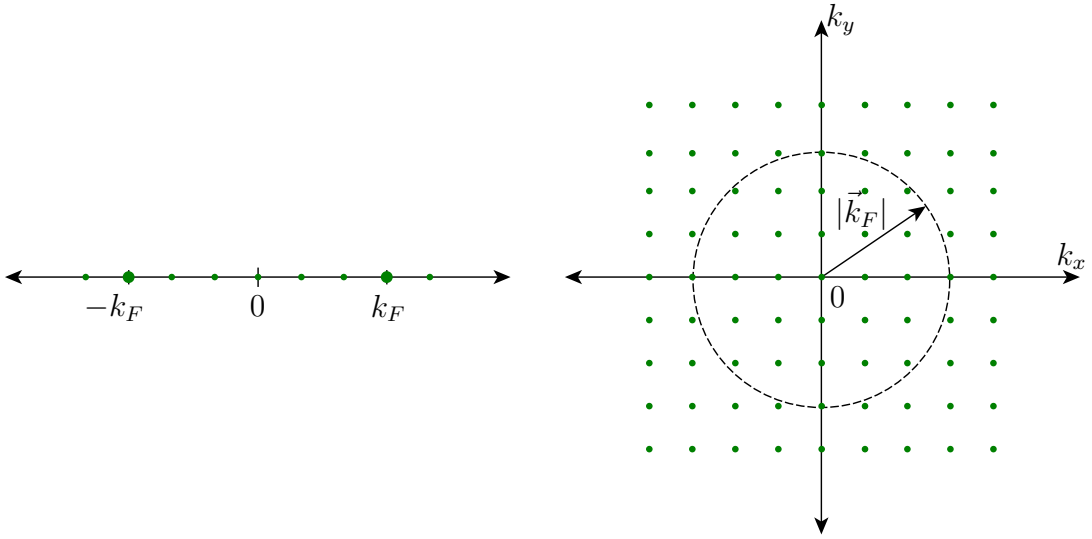

Figure 3.1: Momentum space for 1D- and 2D-systems with discrete momentum states. In the 1D case (left), the Fermi surface consists only of the two points at $k = \pm k_F$ whereas in 2D systems (right) the fermi surface is continuous, in this case collapsing to a circle with radius k_F.

Theoretically, a variety of methods is available to deal with interacting fermions in 1D. It is possible, for example, to apply a perturbative approach with the limitation of weakly interacting systems only. A thorough overview can be found in Ref. [35].
Another, more general approach, is the concept of bosonization, which especially is used for so-called *Tomonaga-Luttinger liquids (TLL)* [38, 39], but not limited to such systems. The main idea behind it is to use bosonic operators to describe fermions, assuming the equivalence between noninteracting bosons and interacting fermions. The TLL picture describes the low energy physics of such systems via parameters similar to the *Landau parameters* in Fermi liquids. There are, however, systems with non-Luttinger behaviour, requiring more sophisticated approaches.
Probably the most successful approach to obtain exact solutions for one dimensional systems is based on the *Bethe ansatz* [40]. Its foundation is the choice of a particular form for the 1D wavefunction suitable to obtain the energy eigenspectrum. Although many models can be solved exactly by exploiting this procedure, they are restricted to systems without an external trapping potential [41]. Furthermore, the resulting expressions tend to be very complicated and often require heavy mathematical analysis in addition to extract physical quantities. In any case, after the initial success of solving the *1D Heisenberg spin chain*, the approach was used to deal with several systems. A review, linking these advances also to experimental progress, can be found in [42].
Despite the availability of several established methods, we have chosen to tackle this problem numerically, by means of the QMC-algorithms discussed in the previous chapter. The reasons are several: first of all, this approach is very general and is not restricted to systems without external potential or zero temperature calculations, like most of the exact methods. Moreover, this approach allows us to exploit established results from the literature as a reliable benchmark and therefore justifies a latter application of the method in more challenging systems, such as higher dimensional models.

In the following, we will introduce the model with its associated scales, discuss results for systems in the ground state and draw a compare to results from the literature, where available.
In 1D we consider the Hamiltonian

$$\hat{H} = -\sum_{k} \sum_{s=\uparrow,\downarrow} \frac{\hbar^2 k^2}{2m} \hat{n}_{s,k} + g \sum_{i} \hat{n}_{\uparrow,i} \hat{n}_{\downarrow,i} \tag{3.1}$$

where the first sum ranges over all occupied momentum states k and the latter sums over all lattice sites i. Although our QMC approach is not limited by these contraints, we will restrict ourselves to unpolarized systems with two particle species, represented by the use of a periodic boundary condition and an equal number of particles $N/2$ in every flavour, respectively. Furthermore we focus on systems without an external trapping potential. Corresponding numerical results relying on the same method for harmonically trapped models, polarized systems, and problems with imaginary chemical potential and mass imbalance can be found in Refs. [44–46].

3.1 Units, scales & dimensions

As typical for ultracold atomic systems, we work in units such that $\hbar = m = k_B = 1$, where m is the mass of the fermions. With these atomic units and the fact that we work in 1D, the coupling g in Eq. (3.1) is connected to the 1D s-wave scattering length a_0 via

$$g = \frac{2}{a_0}, \tag{3.2}$$

with the dimension of an inverse length. In order to obtain a dimensionless quantity to describe the physics, we define consistently with the literature,

$$\gamma = \frac{g}{n}, \tag{3.3}$$

where $n = N/L$ denotes the particle density. In the following, we provide results for multiple values of γ ranging from the weakly attractive region at $\gamma = 0.2$ well into the strongly interacting regime up to $\gamma = 4.0$.
In practice, besides particle number N and the bare coupling g, the effective inverse temperature β and the box-size N_x need to be specified. Although an extrapolation to infinite β needs to be performed to extrapolate to the true ground state, we rely on previously used values for β for which the observables of interest are converged [43]. This allows us to limit the calculations to a few values of β for which we can peform an average to extract the converged result.
We also note, that energies and momenta will be expressed in units of the Fermi energy ϵ_F and the Fermi wavevector k_F in order to present dimensionless quantities. The definitions read as

$$\varepsilon_F = \frac{1}{2} k_F^2 \tag{3.4}$$

and

$$k_F = \frac{\pi}{2}\frac{N}{L}, \tag{3.5}$$

respectively. The definition of the Fermi wavevector is dependent on the dimension and this expression is only valid in 1D.
The lattice-spacing for all subsequent results is set to $\ell = 1$ so that the length of the box is given by $L = \ell N_x$, with N_x being the number of lattice sites. As discussed in the previous section, we discretize the imaginary time into N_τ timesteps via a *Suzuki-Trotter decomposition*. After a thorough investigation of time-discretization effects, we found it sufficient to set the temporal lattice spacing to $\Delta\tau = 0.05$. In the following, we present results obtained by calculating 5×10^4 auxiliary-field configurations and considering every tenth state in order to arrive at 5000 decorrelated samples. This allows us to reach sufficiently small errorbars in the order of $1\% - 2\%$.

3.2 Equal-time density matrices

In the following, we will discuss the one- and two-particle density matrices at equal imaginary time for unpolarized systems. The use of periodic boundary conditions and the absence of external potentials imply spatial translational invariance of the investigated systems. Therefore, we consider $\rho_n(r)$ with $r \equiv |x - x'|$ being the spatial distance. Furthermore, we present the data as a function of $k_\mathrm{F} r$, in order to eliminate the density scale set by k_F. The dimensionless quantity $k_\mathrm{F} r$ can be interpreted as a measure for the interparticle distances, up to a normalization factor.

3.2.1 One-body correlations

Here we discuss our results for the one-body density matrix $\rho_1(x, x')$ which is defined as

$$\rho_1(x, x') = \langle\Omega|\, \hat{\psi}^\dagger_\uparrow(x)\hat{\psi}_\uparrow(x')\,|\Omega\rangle = \langle\Omega|\, \hat{\psi}^\dagger_\downarrow(x)\hat{\psi}_\downarrow(x')\,|\Omega\rangle \tag{3.6}$$

where $\hat{\psi}^\dagger(x)$ and $\hat{\psi}(x)$ denote fermionic creation and anihilation operators and $|\Omega\rangle$ is the projected ground-state, as introduced in Chap. 1.
In Fig. 3.2 we show $\rho_1(k_\mathrm{F} r)$ for $N = 4, 8, 12$ and 16 unpolarized fermions on a 1D lattice with $N_x = 80$ sites. In the weakly interacting regime, at $\gamma = 0.2$, the curves only slightly deviate from the noninteracting curve derived in App. B. The oscillations are a direct consequence of the existence of a Fermi surface, which in 1D corresponds to two points at $\pm k_\mathrm{F}$. Although the oscillations tend to flatten with increasing coupling they stil prevail even at strong coupling, indicating that the feature of the Fermi surface is not entirely lost in this regime. This is further affirmed by the study of the momentum distribution shown further below.
With increasing coupling the curves tend to be moderately more local, suggesting the pairing of fermions. In the limit of infinite attractive interaction the form of the density matrix approaches a delta distribution in the continuum. On the lattice, however, the form

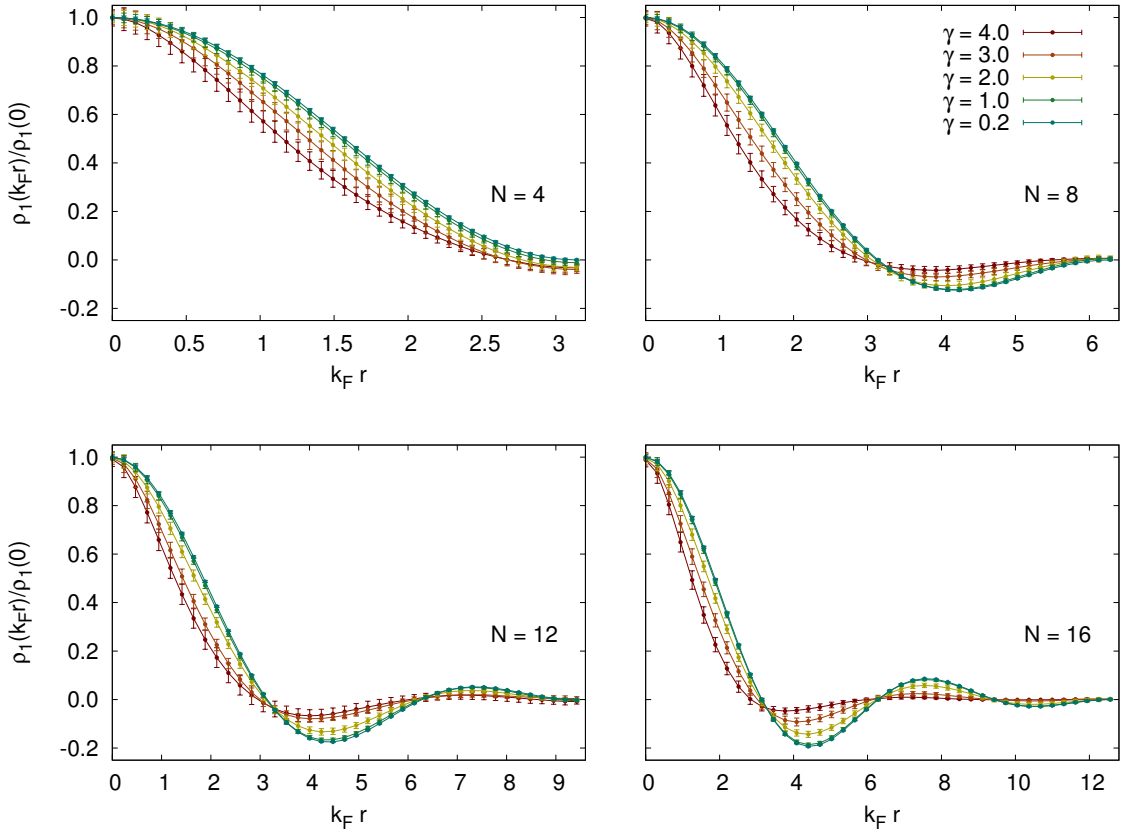

Figure 3.2: The connected points show the single-particle density matrix $\rho_1(k_\mathrm{F}r)$ normalized by $\rho_1(0)$ as a function of $k_\mathrm{F}r$ for several couplings $\gamma = 0.2, 1.0, 2.0, 3.0, 4.0$ and for the particle numbers $N = 4, 8, 12, 16$ at fixed system size of $N_x = 80$.

of this curve deviates from the delta peak due to the introduced UV-cutoff set by the lattice spacing.
As mentioned, the curves corresponding to weakly coupled systems very closely resemble the form $\sin(x)/x$ as it is expected for noniteracting fermions in the continuum. Therefore, we use the expression

$$\rho_1(k_\mathrm{F}r) \approx \frac{N}{2} e^{-ak_\mathrm{F}r} \frac{\sin(k_\mathrm{F}r)}{k_\mathrm{F}r} \tag{3.7}$$

to perform a fit to the data. The fit parameter a is used to interpolate across the coupling strength and is motivated by a similar analysis in 2D. As the coupling increases, it is expected that the functional form in the above expression becomes increasingly influenced by the exponential factor which in the limit of $a \to \infty$ shows the anticipated delta peak. Values for a representative system with $N = 12$ particles are provided in Tab. 3.1.

γ	a	$\sigma(a)$
0.2	0.05	0.006
1.0	0.061	0.006
2.0	0.111	0.004
3.0	0.224	0.008
4.0	0.316	0.011

Table 3.1: Fit parameter a obtained by fitting Eq. (3.7) to the $N = 12$ data of Fig. 3.2, as a function of the dimensionless coupling γ. The rightmost column contains the standard deviation for the fit parameter. These values of a exemplify the typical numbers obtained across all particle numbers.

3.2.2 On-site pair correlation

Additionally to the one-body density matrices we will now discuss our results for the on-site two-body density matrix, i.e. the correlation of zero-size pairs of spin-up and spin-down fermions. The general definition reads

$$\rho_2(x, x') = \langle \Omega | \, \hat{\psi}_\uparrow^\dagger(x) \hat{\psi}_\uparrow(x') \hat{\psi}_\downarrow^\dagger(x) \hat{\psi}_\downarrow(x') \, | \Omega \rangle \,, \tag{3.8}$$

describing the insertion of a fermion pair at x and the annihilation of the same pair at x'. In unpolarized systems the computation of this quantity simplifies greatly since the on-site two body density matrix is given by the square of the one-body quantity after the introduction of the auxiliary fields:

$$\rho_2(x, x') = \int_\mathcal{C} \mathcal{D}\sigma \; P[\sigma] \; [\rho_1(x, x', \sigma)]^2 \tag{3.9}$$

Results for $\rho_2(k_F r)$ are shown in Fig. 3.3, again for the particle numbers $N = 4, 8, 12, 16$ and across couplings from $\gamma = 0.2$ to 4.0. With increasing interaction strength the

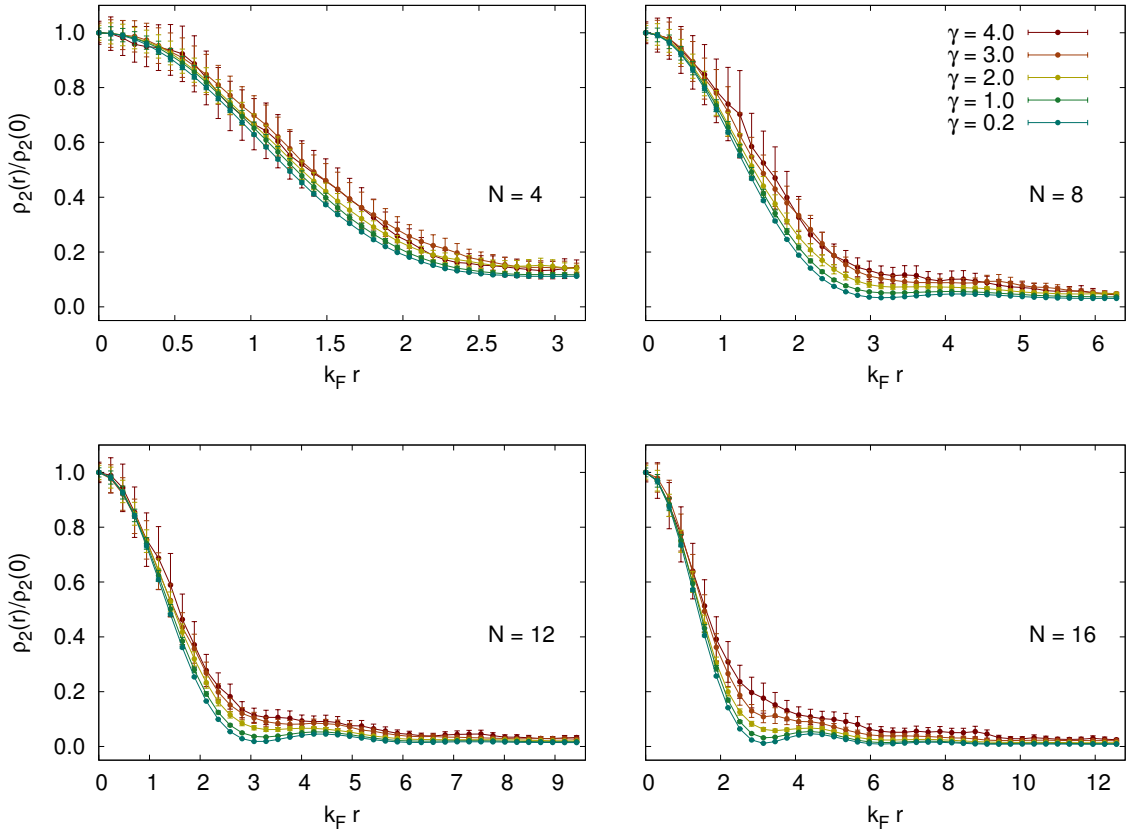

Figure 3.3: Two-body density matrix $\rho_2(k_F r)$ normalized by $\rho_2(0)$ as a function of $k_F r$ for several couplings $\gamma = 0.2, 1.0, 2.0, 3.0, 4.0$ and for the particle numbers $N = 4, 8, 12, 16$ at fixed system size of $N_x = 80$.

fermions get more tightly bound annd form stable composite bosons. It can be seen that these bosons interact repulsively by the slightly more delocalized shape of the curves with increasing interaction. This agrees well with the observations in Ref. [47], which state that the ground-state of strongly attractive fermions can be described by a so-called *super Tonks-Girardeau gas (STG)*.
As apparent from the plots, the results are subject to significantly higher noise, since this is amplified by taking the square of the observable. In principle, one could use higher statistics in order to reduce the statistical error and obtain smoother curves. Here, however, the main interest was to calculate one-body correlations, for which sufficiently small errorbars can be achieved with a similar effort.

3.3 Momentum distribution

In this section we discuss our results for the single-particle momentum distribution n_k defined as

$$n_k = \lim_{k \to k'} \int_0^L dx\, dx' \rho_1(x, x') e^{i(kx + k'x')} \tag{3.10}$$

where $\rho_1(x, x')$ denotes the single-particle density matrix, as defined in Eq. 3.6. Since we are working on a 1D lattice in real space, the corresponding allowed values for the momenta are discretized to $k_j = 2\pi j / L$.
In Fig. 3.4, our results for systems of $N = 4, 8, 12$ and 16 particles at a fixed lattice with $N_x = 80$ sites are shown. Further, we investigate the weakly interacting regime starting at $\gamma = 0.2$ and move progressively to the strongly attractive region up to $\gamma = 4.0$. In the limit of the noninteracting case the momentum distribution features a discontiuous drop at $k = k_\mathrm{F}$ which is still clearly visible for the weakly coupled curves. States with momenta $k > k_\mathrm{F}$ are occupied for increased couplings, however, the curves still feature a relatively sharp drop above the Fermi wavevector. Although the concept of a Fermi surface does not apply in 1D, the effect is similar to higher dimensions: below a certain value of k states are mostly occupied whereas states with higher momenta a much less likely. Moreover, we observe that this structure is altered only moderately and the Fermi wavevector still provides the scale in the strongly coupled regime. This shows that even in the strongly coupled systems, fermion pairing predominantly includes states in the vicinity of the Fermi points.
As mentioned before, the allowed values for the momentum are discretized here, and the amount of momentum states below the Fermi surface is proportional to the number of particles in the system. This limits the resolution of low-density systems ($N = 4$) and we therefore can not fully characterize the smoothing in the vicinity of the fermi vector, as it would be possible with continuous or analytic approaches.

3.4 Contact parameter

We will now present our results for the contact parameter C, which is a measure of the fermion-pairing in the system. It can be shown analytically [22], that the high-momentum

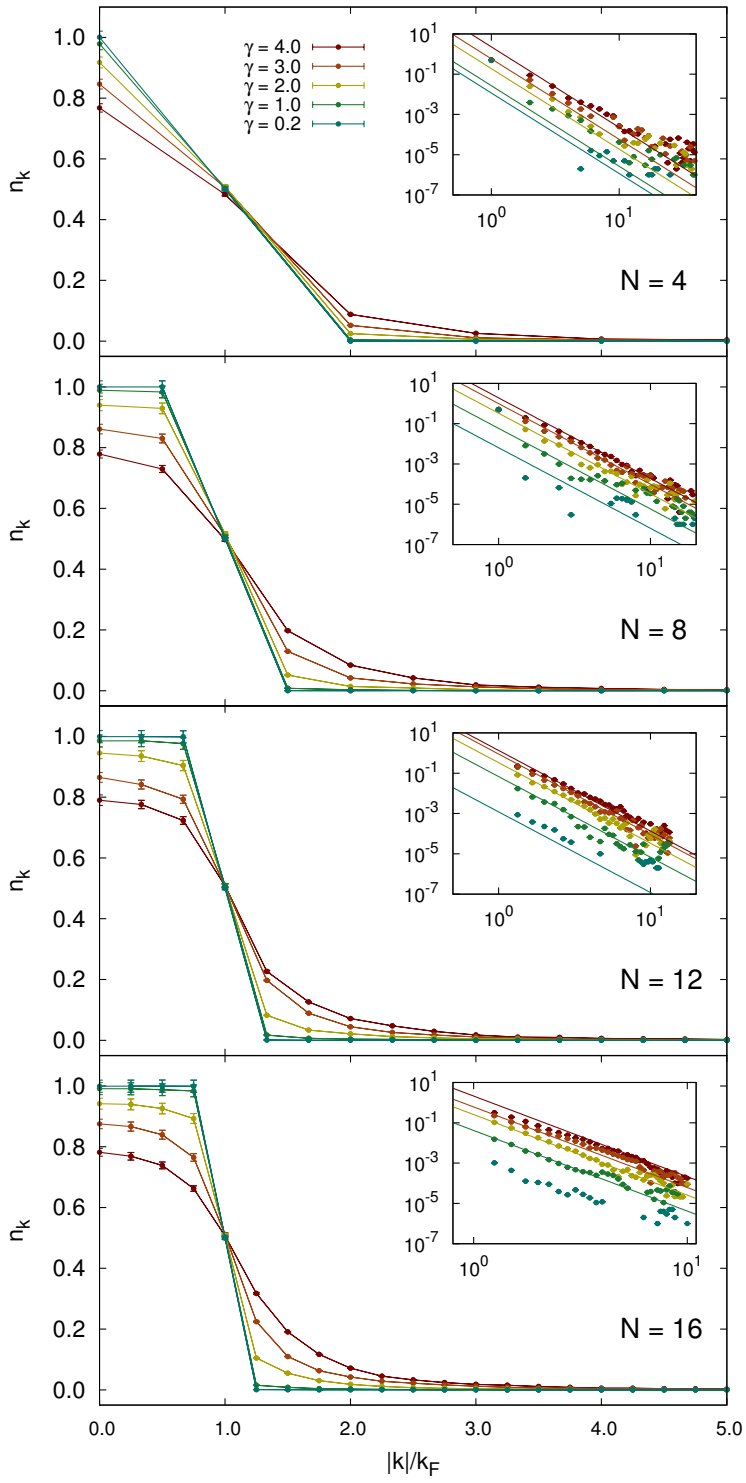

Figure 3.4: Momentum distribution n_k as a function of $|k|/k_F$ for $N_x = 80$ lattice sites and particle numbers $N = 4, 8, 12, 16$. The inset shows the asymptotic behaviour in a log-log scale, solid curves represent a linear fit used to extract the contact paramter.

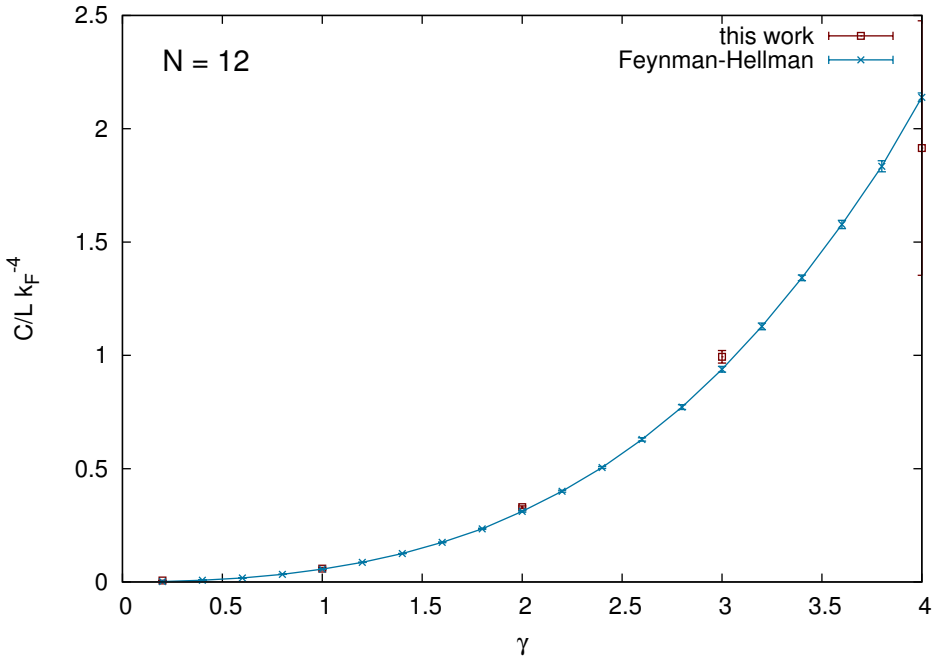

Figure 3.5: Contact density obtained from the C/k^4 decay in the momentum distribution (red) compared to results obtained from [43] (blue) for a representative few-body system with $N = 12$ particles at a fixed lattice size of $N_x = 80$.

tail of the momentum distribution obeys the law

$$n_k \approx \frac{C}{k^4}. \tag{3.11}$$

Considering Eq. (3.11), we can extract C by applying a fit of the form $n_k = bx^4$ to the high momentum part of the momentum distributions obtained earlier. To avoid a systematic underestimation originating from the plateau at values $|k| < k_F$, we typically consider the region $|k|/k_F \gtrsim 2.0$ for the fits, which is remarkably close to the value used in studies for 3D systems [48]. In principle there should not be any further constraints on the momentum tail but, as evident from the insets of Fig. 3.4, the asymptotic part of the momentum tail is subject to heavy noise due to lattice artifacts. Therefore, we need to chop off this part of the decay at $|k|/k_F \approx 8.0$ in order to stabilize the fitting procedure. In Fig. 3.5 we show the contact density as a function of the dimensionless coupling γ. We see a rising contact density as the attractive coupling increases, which reflects the expectation to find more tightly bound pairs in strongly interacting systems. Furthermore, C is compared to results calculated in an earlier study using the Feynman-Hellman relation discussed in Sec. 1.4. In general, we observe a good agreement between the methods, although our result differs slightly in the strongest coupled case. This, again, is an effect originating from the fact that we work on the lattice, which especially becomes problematic in the strongly coupled regime due to the achievable resolution for tightly bound pairs.

3.5 Finite volume effects

A very important point to consider in numerical calculations is the finiteness of the observable systems. Although the infinite volume can be mimicked - to a certain extent - by the use of periodic boundary conditions, one still needs to perform extrapolations to obtain the desired physical quantity. In Fig. 3.6 we show this effect in the momentum distribution for two representative systems of $N = 16$ particles. As apparent from Fig. 3.6, there is no noticable finite volume effect for systems with γ set to 0.2, representing the free case up to a very small deviation. In the strongly interacting regime on the other hand, the finite volume effect is more pronounced, yet straightforward to control. Starting out at $N_x = 20$, gradually higher volumes were taken into account until a sufficient convergence at a system size of $N_x = 80$ was achieved.
Evidently, the momentum distribution is not the only quantity influenced by finite size effects. Other computed quantities, such as the density matrices, however, feature the very same type of convergence and, hence, will not be considered separately at this point.

3.6 Finite imaginary time

As mentioned in the beginning, we evaluate expectation values up to a finite value of the imaginary time, which would correspond to a finite effective inverse temperature. Since our approach exploits an inital guess state (in our case taken to be a Slater-determinant) and projects to the ground state, we need to make sure that the obtained results are fully converged to the limit $\beta \to \infty$. In Fig. 3.7 we show this effect for two systems in the weakly and strongly interacting regime. In order to minimize computational effort, the lower bound of $\beta\epsilon_F$ was chosen to be 0.65, as motivated by results for the ground state energy from Ref. [43]. Again, as expected, the (almost) free case at $\gamma = 0.2$ shows no dependence on β and is converged almost immediately, whereas strongly interacting systems need longer projection times to be converged to the approriate limit. As depicted in Fig. 3.7, we find a reasonable convergence for $\beta\epsilon_F = 2.5$ in the latter case and therefore we use this value throughout this work.

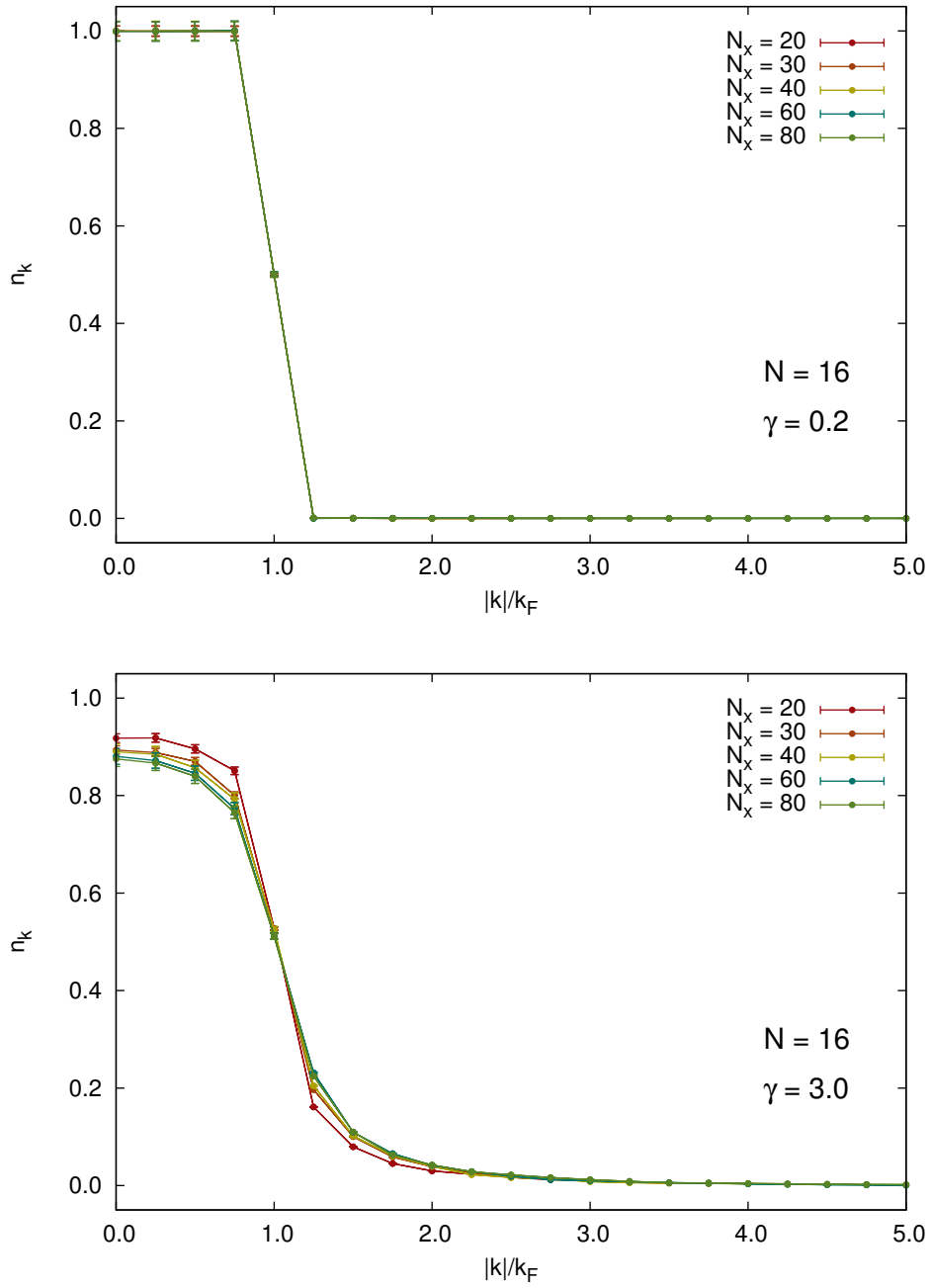

Figure 3.6: Momentum distribution for values of the box size $N_x = 20, 30, 40, 60$ and 80. The top panel shows the very weakly coupled case of $\gamma = 0.2$. Strongly coupled systems at $\gamma = 3.0$ are shown in the lower panel. Clearly, finite volume effects are more pronounced in the latter case.

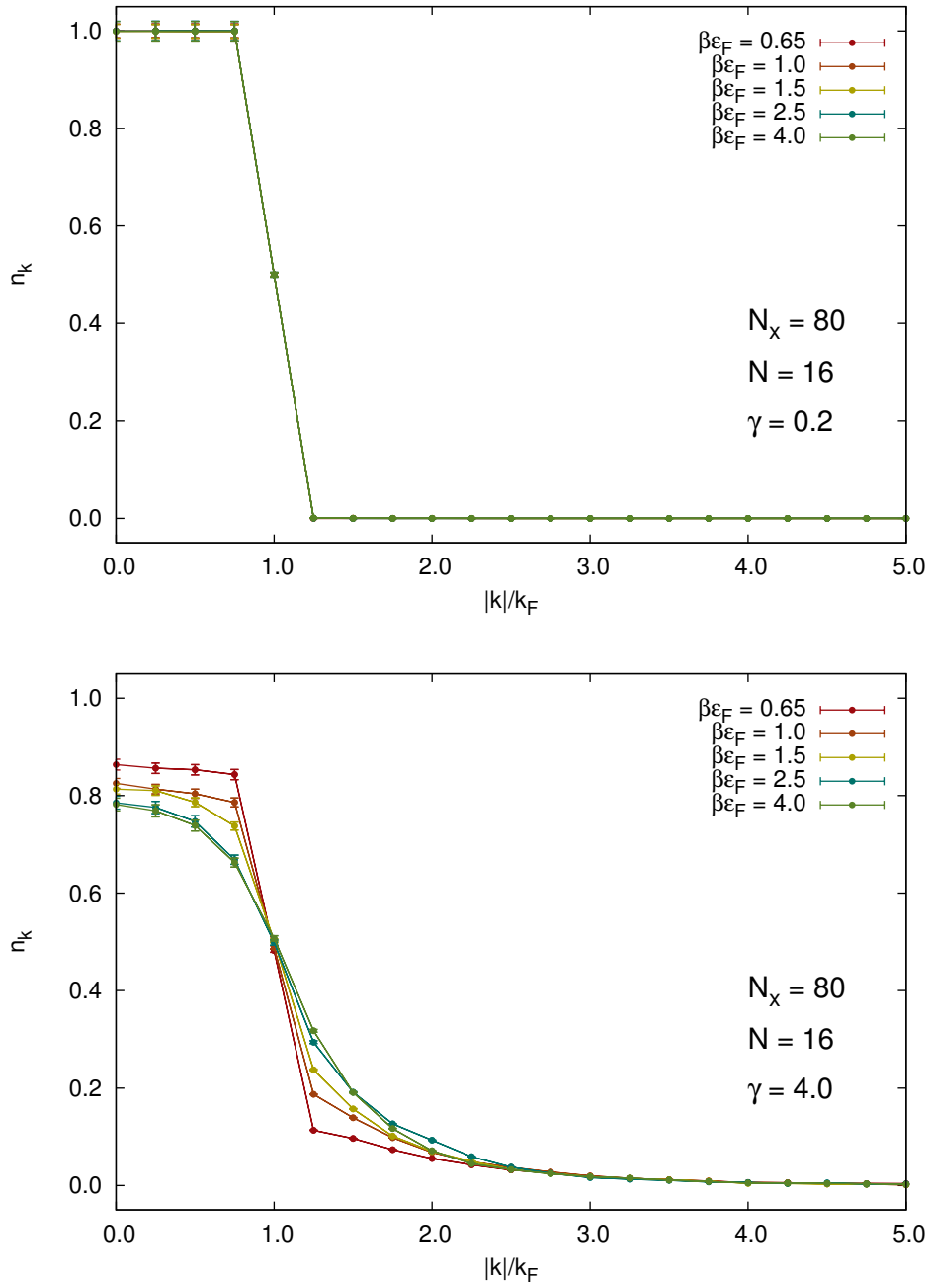

Figure 3.7: Momentum distribution for values of the imaginary time $\beta = 0.65, 1.0, 1.5, 2.5$ and 4.0. The weakly interacting system with $\gamma = 0.2$, shown in the top plot, seems to be immediately converged. In the strongly correlated case at $\gamma = 4.0$, shown in the bottom plot, convergence is achieved at $\beta\epsilon_F = 4.0$.

Chapter 4

The two-dimensional Fermi gas

In a similar fashion as for the 1D case, we will now analyze the ground-state of nonrelativistic, two-dimensional (2D) Fermi gases on a lattice. In particular, we focus on the crossover from Bardeen-Cooper-Schrieffer (BCS) pairing in the weakly coupled regime to Bose-Einstein condensation (BEC) on the strongly interacting side.
As discussed before, 1D models can be treated effectively by numerical means and sometimes are even solvable analytically. On the other hand, mean-field theory can accurately capture results for many aspects of the physics in three- or even higher-dimensional systems, because the effect of correlations beyond mean-field diminishes with increasing dimension. Two-dimensional systems represent, thus, the challening middleground between "accessible" dimensions: the observed effects are often strongly influenced by both thermal and quantum fluctuations. This raises the need for very careful numerical calculations for strongly correlated fermions in a 2D confinement.
As in the previous sections, we focus on unpolarized systems in the dilute limit with periodic boundary conditions. We characterize the system via the one-particle density matrix at equal imaginary times. Moreover, we present equations of state for the total and interaction energies in the crossover from few- to many-body systems. Again, finite size effects need to be investigated to ensure the validity of the obtained results and to justify an extrapolation the continuum limit (CL).

Parts of the following discussion and results have been already published in the APS Journal "Physical Review A": **93**, 033639 (2016) (see Ref. [49]).

Recently, it became possible to realize two-dimensional Fermi gases experimentally in a controllable and precise way [50, 51]. These advances make it possible to understand several fundamental aspects of the few- and many body physics generic to 2D quantum mechanics, which exhibits many exciting effects.
A central phenomenon of interest is the fermion pairing, because it is responsible for superconducting and superfluid behaviour. The stability of the superfluid phase is correlated with the robustness of the fermion pairs, which is determined, in turn, by the interaction strength, i.e. the s-wave scattering length. As opposed to 3D, two-body bound states always are present in 2D systems, even for arbitrarily small interaction strenghts. Strictly speaking, pair condensation can only occur at $T = 0$, as dictated by the *Mermin-Wagner theorem* [52–54], which states that continuous symmetries in 2D systems cannot be spontaneously broken at finite temperature (with sufficiently short-ranged interactions). Nev-

ertheless, a superfluid phase can actually be observed below a critical temperature T_c, where the system ungergoes a Berezinskii-Kosterlitz-Thouless (BKT) transition [55–57]. The great interest in such systems is especially motivated by the belief that unconventional high-temperature superconductivity in cuprates is essentially a 2D effect [58]. Therefore, a lot of experimental effort has been put forward to find materials with a strong pairing mechanism. The formal description of 2D Fermi gases, however, is mostly limited to numerical studies, since analytic tools to treat this problem are very scarce at this time [59]. For the earliest theoretical investigaion of the crossover from BCS to BCS pairing, mean-field methods were used [60,61]. Such an approch is problematic, since in 2D systems observables are highly influenced by quantum- and thermal fluctuations. The former could be captured, as for ther local part, by means of DMFT calculations [62, 63] although the predominant (spatial) part of the fluctuations was still neglected. In the last decade, however, progress was achieved to include spatial correlations beyond DMFT in 2D by means of cluster [64–66] and diagrammatic [67–73] extensions of DMFT. So far, their application was mostly restricted to the case of repulsive interactions and finite temperature. Thus, for 2D systems, the most widespread treatement is usally based on Monte Carlo schemes. In particular, studies based on the diffusion Monte Carlo method improved the poor accuracy of the mean-field estimates for the ground-state energy and also computed the contact parameter [74]. This approach [75], as well as auxiliary field Monte Carlo methods [76], was used to further characterize the ground-state of polarized and spin-imbalanced systems. Moreover, energies and contact at finite temperature as well as the the BKT-transition point have been explored [77–79].
Thus, some light has been shed on the ground-state of 2D Fermi systems. However, most of this calculations were done at high particle numbers, i.e. in the "many-body" regime. Hence, much less information about the behaviour at low particle numbers and the convergence to the thermodynamic limit is available. It is the purpose of the work presented in this chapter, to fill this gap.
Since we are considering dilute gases, the interaction can be modeled as a zero-range potential. Therefore, our Hamiltonian can be written as

$$\hat{H} = \hat{T} + g\hat{V}, \tag{4.1}$$

where

$$\hat{T} = -\frac{\hbar^2}{2m} \sum_s \sum_{\vec{k}} \hat{\psi}^\dagger_{s,\vec{k}} \hat{\psi}_{s,\vec{k}} \tag{4.2}$$

constitutes the kinetic term and the potential part is given by

$$\hat{V} = \sum_i \hat{n}_{\uparrow,i} \hat{n}_{\downarrow,i}. \tag{4.3}$$

where the lattice spacing ℓ was set to 1. The index s denotes spin-species, ranging over the values $s =\uparrow$ and $s =\downarrow$ with an equal number of $N/2$ particles per flavour. Further, $\hat{\psi}^\dagger_{s,i}$ and $\hat{\psi}_{s,i}$ are fermionic creation- and anihilation operators at lattice site i, respectively. As usual, $\hat{n}_{s,i} = \hat{\psi}^\dagger_{s,i}\hat{\psi}_{s,i}$ denotes the associated particle density. In the following, we compute many essential properties to describe the crossover between few- and many-body physics

in such systems.

4.1 Units, scales & dimensions

As in the 1D calculations, we present all our results in dimensionless quantities. Energies are therefore rescaled with the energy of the noninteracting gas on the lattice

$$E_{\mathrm{FG}} = \frac{1}{2} N \varepsilon \mathrm{F} \tag{4.4}$$

whith particle number N and Fermi energy ε_{F}. The definition of the latter reads the same as in 1D

$$\varepsilon_F = \frac{1}{2} k_F^2 = \pi n \tag{4.5}$$

whereas the occuring Fermi wavevector differs from the expression in 1D and is given in 2D by

$$k_F = \sqrt{2\pi n} = \sqrt{2\pi \frac{N}{L^2}}. \tag{4.6}$$

By setting the units $\hbar = m = k_B = 1$, as already done in the one-dimensional case, we notice that the bare coupling g in Eq. (4.1) becomes dimensionless. Thus, no dimensionful parameters enter the dynamics of the system, making it *classically scale invariant*. This invariance, however, is broken by quantum fluctuations, resulting in a non-zero binding energy of the two-body problem, which we can use as a physical scaling parameter instead. Since the bare coupling is a direct input to the calculation, we need to provide a mapping between g and the associated binding energy ε_{B} of the two-body problem. It is therefore necessary, to numerically compute ε_{B} as a function of g. Furthermore, in order to investigate systematic grid-size effects, the calculation of ε_{B} has to be performed for each lattice size separately. We found, however, that for the two-body problem these effects are negligible implying that the binding-energy on the lattice solely depends on the bare coupling g.
For the sake of conciseness, the dimensionless coupling η is introduced, defined as

$$\eta \equiv \frac{1}{2} \ln\left(\frac{2\varepsilon_F}{\varepsilon_B}\right). \tag{4.7}$$

This definition is consistent with the literature and η is constructed such that the BCS-regime is approached with a large positive value of η. Large negative values of η mark the BEC area, where the binding-energy dominates the scale. In Fig. 4.1, the map between η, i.e. the binding energy, and the bare coupling is shown across the BCS-BEC crossover. It is apparent that an increase of the system size favors lower bare couplings. Although larger systems take a longer computation time, the lowered value of g allows us to use a more coarse time-discretization length $\Delta\tau$, which, in turn, lowers the numerical effort. The opposite effect takes place for systems with the particle content, which correlates with a higher value of g. Therefore, the numerical effort increases significantly, since

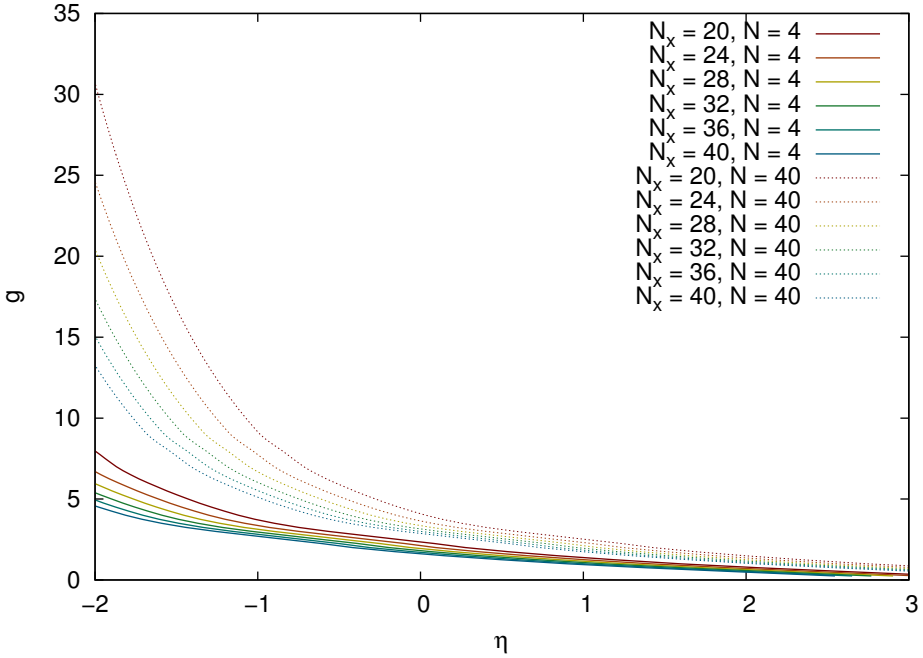

Figure 4.1: Bare coupling g as a function of the dimensionless coupling η for a particle number of $N = 4$ and $N = 40$. Higher particle numbers correspond to increased values of g at the same coupling η, whereas the increase of the lattice size N_x shows an opposite trend.

the computation time already scales linearly with N. This has the implication that such calculations are limited to dilute systems.
The lattice properties are unchanged with respect to the 1D calculations presented in the previous chapter, aside from the fact that the calculation now scales with N_x^2 due to the increased dimensions. The time-discretization has been extensively studied due to the exponential increase of the bare coupling with decreasing η. Systems with a coupling of roughly $\eta \approx 0.5$ or higher are treatable with a temporal spacing of $\Delta\tau = 0.05$, where the exact cutoff in η depends on the system size and particle content. Calculations for systems with a value of $0.5 < \eta < -2.0$ can be performed with $\Delta\tau = 0.01$ within a reasonable computational time. In principle, even stronger couplings are tractable with a finer timestep, with the effect of an exponential increase of computational effort. To characterize the BCS-BEC crossover, we found it sufficient to calculate results for couplings in the interval $\eta \in [-2.0, 3.0]$ and therefore limit ourselves to a time-discretization length of $\Delta\tau = 0.01 - 0.05$.
The number of samples was fixed to 500, where again every tenth accepted configuration in the Markov-sequence was considered as a decorrelated sample, as done in 1D. This allows us to calculate quantities up to a uncertainty of roughly 5%, yielding an acceptable estimate for the energies, momentum distributions and density matrices, which are computed for the first time in the 2D few- to many-body crossover.

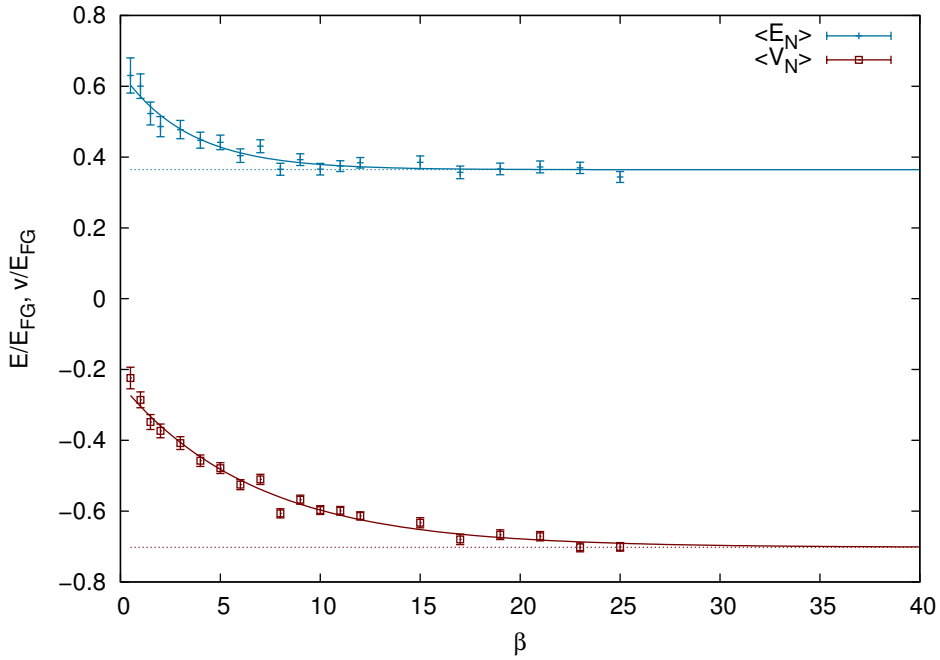

Figure 4.2: Decay as a function of β of the total and interaction energies (in units of E_{FG}) for $N = 20$ particles on a 28×28 lattice, coupled with $\eta = 1.0$. The interaction energy $\langle V \rangle$ takes slightly longer to decay to a plateau.

4.2 Energetics of the ground state

In this section, we present results for an *equation of state (EOS)* of the system, connecting the number of particles with the total and interaction energies of the ground-state. In particular, we characterize the BCS-BEC crossover for several particle numbers, starting in the few-body case at $N = 4$ particles ranging well into the many-body regime up to $N = 40$ particles extrapolated to an infinite lattice size. In the latter case, our results are within reasonable agreement with erlier studies carried out in the *thermodynamic limt* [74].

4.2.1 Extrapolations

Unlike in the 1D case, where useful parameter values for the convergence of observables are available, there is hardly any prior information accessible for 2D systems [77]. For this reason, the exploration of the parameter space proved to be very challenging due to the extended computational effort as compared to 1D calculations. Since the EOS only considers the dependence on the particle number N for various couplings η, we need to eliminate all other scales, namely the large time β and the volume $V = N_x^2$.

Large effective inverse temperature

First, we need to make sure that the results are converged to the true ground state by taking the limit

$$\langle \mathcal{O} \rangle = \lim_{\beta \to \infty} \langle \mathcal{O}(\beta) \rangle. \tag{4.8}$$

Carrying out calculations at increasing imaginary times β, we can perform a fit of the form

$$E(\beta) \approx E_0 + a e^{b\beta}, \tag{4.9}$$

as motivated by the derivation in App. A. In Fig. 4.2 we show the typical convergence behaviour of the total and interaction energies for a representative system of $N = 20$ particles at a 28×28 lattice coupled with $\eta = 1.0$. At very low effective inverse temperature the data slightly deviates from the proposed form in (4.9). After a certain value of β, strongly depending on the system parameters, the neglected effects in the derivation vanish and the computed data decays as expected. In the BCS-BEC crossover region at around $\eta = 0.5$, this extrapolation requires the computation of data up to significantly larger β due to a slow decay. This reflects the use of a Slater-determinant as the initial guess-state, which is the best choice, close to the noninteracting case. The stronger the interaction, the more the actual ground-state wavefunction will deviate from such a trial state. This explains the slower decay. In principle, this effect could be minimized by a better choice of the initial guess-state, e.g. by a coupling dependent interpolation between a BCS and a Jastrow-Slater (JS) trial wavefunction [80]. The use of a trial wavefunction which is not in the form of a determinant, however, greatly changes the method introduced in Sec. 2.2 since e.g. the probability measure cannot be expressed as a determinant in such a case. Furthermore, at very high couplings in the region $\eta \leq -1.0$, the interaction is strong enough to overcome this issue and favors a fast decay to the ground-state. For this reasons, we found it sufficient to use a Slater determinant as our noninteracting guess state for a first characterization of such systems.
Fig. 4.4 additionally shows the decay of the interaction energy for the same system. Although this follows the same functional form as the total energy, we note a slower convergence in imaginary time. As a result, the extraction of the converged values becomes more challenging which is reflected by slightly larger errors for the obtained values.

Infinite volume

With the data extrapolated to the ground-state ($\beta \to \infty$), we can now eliminate the volume scale by another extrapolation. Therefore, we need to look at the data as a function of the inverse volume ($V^{-1} = N_x^{-2}$) and perform a fit of the form

$$E(V^{-1}) = a + bV^{-1}. \tag{4.10}$$

The value at vanishing inverse volume represents the extrapolated result in the infinite volume limit, i.e. the dilute limit at constant particle number. The fit parameter a then corresponds to the value in this limit. In Fig. 4.3, curves for representative calculations in the BCS and BEC regimes are shown.

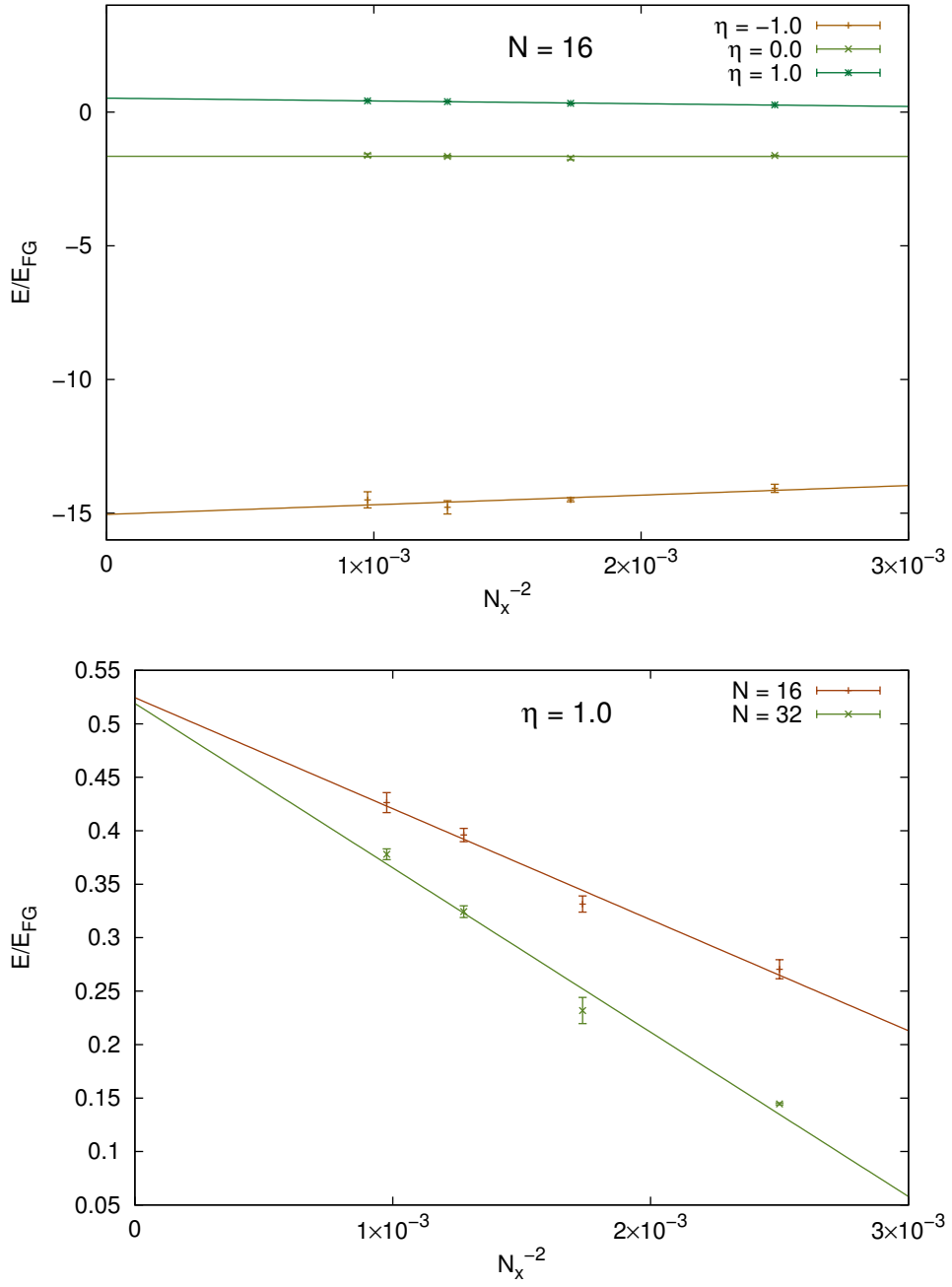

Figure 4.3: Top: Extrapolation of the ground-state energy to the infinite volume limit for $N = 16$ unpolarized fermions, as a function of $V^{-1} = N_x^{-2}$, for several values of the dimensionless coupling $\eta = -1.0, 0.0, 1.0$. Bottom: Comparison of the extrapolation for the ground-state energy for different particle content $N = 16, 32$ at fixed coupling $\eta = 1.0$. (Reproduced from Ref. [49])

4.2.2 Equation of state

After extrapolating the lattice results to the appropriate limits, we now discuss these quantities as a function of the remaining parameters of interest. In the following, we show how the ground-state and interaction energies are behaving with increasing particle content starting in the few-body regime at $N = 4$. Gradually increasing the particle number up to a value of $N = 40$ displays a convergence to the many-body limit across all investigated couplings.

Ground-state energy

Fig. 4.4 displays the computed ground-state energy as a function of particle number. To show the molecular structure of the fermions, the binding energy ε_{B} is used as a scale in the BEC limit. In the weakly interacting BCS regime, we show the results in units of the energy of the noninteracting system E_{FG}.
To compare these results with the literature, values from Ref. [76] are shown at a value of $N = 50$. Strictly speaking, the values correspond to infinite particle number since the thermodynamic limit is reached by taking $N \to \infty$ and $V \to \infty$ at constant density $n = N/V$. We formally approach this limit by taking the dilute limit for each particle number separately and present these values as a function of N. As evident from Fig 4.4, the few-body results converge to the TL at a particle content of $N \approx 24$, consistent with observations in Ref. [74] and even at lower particle numbers for very strongly coupled systems. The values for the highest populated systems show very good agreement with the TL results, indicating that we have reached the many-body regime.
In addition to the interacting results, a curve for the noninteracting system ($\eta = \infty$) on the lattice is shown. The structure of this curve resembles the oscillations of the lowest coupled systems, which originate from so-called *closed-shell (CS)* effects, discussed more extensive below.
Curves for the strongly interacting regime are shown in the bottom panel, where we see a clear dominance of the binding-energy. This indicates that tightly bound pairs form immediately upon turning on the interaction.
More importantly, the curves corresponding to the BCS-BEC transition region, at $\eta = 0.5$ and $\eta = 1.0$, still show covergence in the particle number. The calculation for these parameters becomes numerically very challenging, due to the choice of the initial guess state $|\Omega_o\rangle$. As mentioned above, these values could in principle be refined by a more suitable choice of the initial wavefunction, which would lower the numerical effort significantly, allowing a determination of observables at even higher particle numbers within a reasonable computational time.
The numerical results plotted in Fig. 4.4 are provided in Tab. 4.1.

Interaction energy

To further characterize the properties of the ground-state, specifically its short-range behaviour, we present the expectation of the potential part $\hat{V}$ of the Hamiltonian, denoted as $\langle \hat{V} \rangle_{\mathrm{N}}$ at fixed particle number N. As shown in Sec. 1.4 we can use the Feynman-Hellman

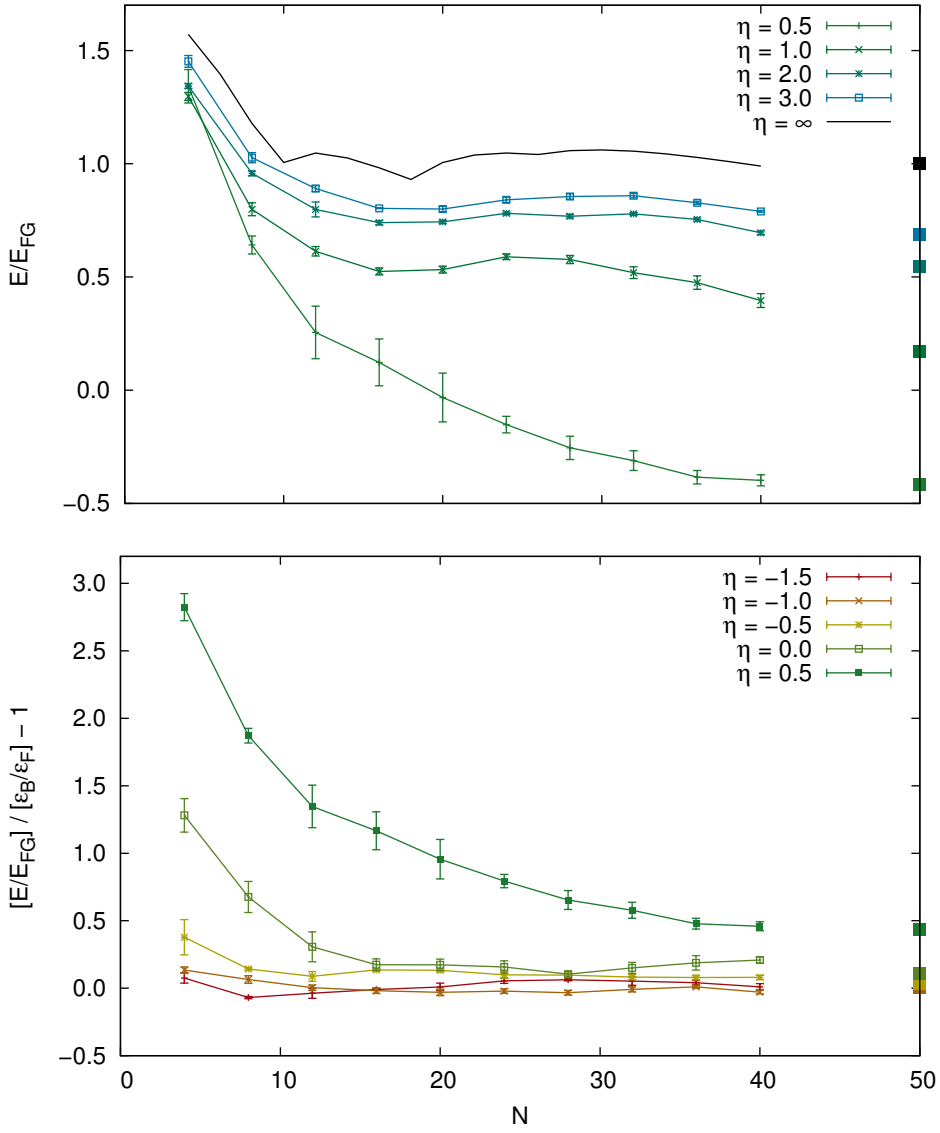

Figure 4.4: Ground-state energy E of $N = 4, 8, 12, ..., 40$ unpolarized fermions, for several values of the dimensionless coupling $\eta = -1.5, -1.0, \ldots, 3.0, \infty$, the final corresponding to a free system. All values are extrapolated to the limits of $\beta \to \infty$ and $N_x^{-2} \to \infty$. The top panel shows E for the four weakest couplings we calculated, in units of the energy of the noninteracting system. The bottom panel displays E for the strongest couplings we considered, using the binding energy per particle $\varepsilon_B/2$ as a scale. Clearly, for $\eta < 0$ the energy per particle is dominated by the pair binding energy across all particle numbers. In both plots, the ground-state energy results of Ref. [76] in the thermodynamic limit are shown with solid squares at $N = 50$. (Reproduced from Ref. [49])

	η								
N	-1.5	-1.0	-0.5	0.0	0.5	1.0	2.0	3.0	∞
4	-37(2)	-12.8(3)	-3.4(7)	0.6(2)	1.34(7)	1.30(2)	1.34(1)	1.45(3)	$\pi/2$
8	-43.0(3)	-13.8(4)	-4.66(5)	-0.6(2)	0.64(4)	0.80(3)	0.96(1)	1.03(2)	$3\pi/8$
12	-41(2)	-14.7(3)	-5.0(2)	-1.4(2)	0.3(1)	0.61(2)	0.80(3)	0.89(1)	$4\pi/12$
16	-40.6(2)	-15.0(3)	-4.70(4)	-1.65(9)	0.1(1)	0.52(2)	0.74(1)	0.80(0)	$5\pi/16$
20	-39(1)	-15.2(4)	-4.72(6)	-1.65(9)	-0.0(1)	0.53(2)	0.74(1)	0.80(1)	$8\pi/25$
24	-38.0(8)	-15.1(2)	-4.9(1)	-1.69(9)	-0.15(4)	0.59(1)	0.78(0)	0.84(1)	$4\pi/12$
28	-37.6(3)	-15.3(2)	-4.91(8)	-1.79(4)	-0.25(5)	0.58(2)	0.77(1)	0.86(1)	$33\pi/98$
32	-38(1)	-14.9(3)	-4.99(1)	-1.70(8)	-0.31(4)	0.52(3)	0.78(1)	0.86(1)	$43\pi/128$
36	-38.5(6)	-14.6(1)	-5.01(7)	-1.6(1)	-0.38(3)	0.48(3)	0.75(1)	0.82(0)	$53\pi/162$
40	-39.8(9)	-15.2(2)	-5.00(9)	-1.58(4)	-0.40(2)	0.40(3)	0.70(0)	0.80(1)	$63\pi/200$

Table 4.1: Ground-state energy E on the lattice, in units of the continuum noninteracting energy $E_{\text{FG}} = N\varepsilon_F/2$ of the N-particle system, as a function of N and the dimensionless coupling η. (Reproduced from Ref. [49])

relation to write

$$\langle \hat{V} \rangle_{\text{N}} = \left. \frac{\partial E}{\partial g} \right|_{N=\text{const}} . \tag{4.11}$$

This relation is connected to the contact, which fulfills an adiabatic theorem [81] and is therefore proportional to the change in the ground-state energy with respect to the s-wave scattering length a_0 at fixed particle content:

$$C \propto \left. \frac{\partial E}{\partial \ln(k_{\text{F}} a_0)} \right|_{N=\text{const}} . \tag{4.12}$$

The scattering-length controls the behaviour of the system via the UV-lattice cutoff and the bare coupling g. Since the former is held constant, we only need to consider the effect of g in the derivative. Rewriting Eq. (4.12) to

$$\left. \frac{\partial E}{\partial \ln(k_{\text{F}} a_0)} \right|_{N=\text{const}} = \left. \frac{\partial E}{\partial g} \frac{\partial g}{\partial \ln(k_{\text{F}} a_0)} \right|_{N=\text{const}} = \langle V \rangle_{\text{N}} \left. \frac{\partial g}{\partial \ln(k_{\text{F}} a_0)} \right|_{N=\text{const}} \tag{4.13}$$

yields a form which splits into two parts. The second factor in Eq. (4.13) only depends on two-body physics, since we used the binding-energy, i.e. the scattering length, to fix the desired value of g while the first factor contains valuable information about the short-ranged behaviour of the ground-state mandy-body problem.
In Fig. 4.5, results for $\langle \hat{V} \rangle_{\text{N}}$ are shown as a function of particle number and coupling. Again, the results are scaled with E_{FG} so that the values effectively represent the interaction energy per particle. As expected, $\langle \hat{V} \rangle_{\text{N}}$ increases greatly with the interaction strength, suggesting more tightly bound pairs as η approaches the BEC-limit. Further, we note convergence to a plateau as the particle content increases, which is especially evident for the weakly coupled systems under consideration.

	η								
N	-1.5	-1.0	-0.5	0.0	0.5	1.0	2.0	3.0	∞
4	-39(2)	-19.7(6)	-7.0(7)	-1(1)	-0.1(2)	-0.34(5)	-0.50(1)	-0.6(2)	-1/(2π)
8	-28(2)	-15(1.5)	-7.9(7)	-2.7(5)	-0.86(9)	-0.55(9)	-0.41(1)	-0.5(1)	-1/(2π)
12	-21(2)	-14.1(9)	-7.8(3)	-4.0(1)	-1.47(4)	-0.59(1)	-0.42(4)	-0.44(7)	-1/(2π)
16	-17.7(1)	-12.2(5)	-6.8(1)	-3.9(1)	-1.2(2)	-0.58(1)	-0.38(2)	-0.43(2)	-1/(2π)
20	-16(1)	-11.7(6)	-6.8(3)	-3.8(1)	-1.44(8)	-0.59(4)	-0.41(2)	-0.52(6)	-1/(2π)
24	-14.0(9)	-10.4(6)	-6.4(3)	-3.8(1)	-1.55(1)	-0.60(1)	-0.41(1)	-0.50(5)	-1/(2π)
28	-12.5(9)	-9.5(6)	-6.0(4)	-3.6(2)	-1.67(3)	-0.64(1)	-0.44(1)	-0.48(5)	-1/(2π)
32	-11.4(9)	-8.5(6)	-5.6(3)	-3.4(1)	-1.68(1)	-0.69(4)	-0.41(1)	-0.46(4)	-1/(2π)
36	-11.5(1)	-8.4(6)	-5.6(3)	-3.3(1)	-1.65(1)	-0.68(3)	-0.40(2)	-0.45(4)	-1/(2π)
40	-10.5(9)	-8.0(6)	-5.4(3)	-3.1(1)	-1.59(2)	-0.71(3)	-0.41(2)	-0.43(3)	-1/(2π)

Table 4.2: Ground-state interaction $\langle \hat{V} \rangle_{\mathrm{N}}$, in units of the energy of the noninteracting gas E_{FG}, as a function of N and the dimensionless coupling η. (Reproduced from Ref. [49])

The numerical values for $\langle \hat{V} \rangle_{\mathrm{N}}$ are presented in Tab. 4.2.

Shell effects

As mentioned before, in Fig. 4.4 we observe mild oscillations in the ground-state energy for weakly coupled systems. This is a direct consequence of the Pauli exclusion principle, which can be demonstrated by considering the noninteracting Fermi gas. The single-particle states in this case reduce to plain waves with momentum

$$\vec{k} = \vec{k}_x + \vec{k}_y. \tag{4.14}$$

Within an isotropic lattice, i.e. the lattice spacing does not depend on the direction, it is obvious, that multiple combinations of k_x and k_y, yielding the same energy contribution $E_{\vec{k}} = \frac{\vec{k}^2}{2}$, exist. In order to populate the system with $N/2$ particles in every spin-flavour, gradually higher energy levels up to the Fermi energy, are occupied. For some values of N, states which preserve the square symmetry in $\vec{k}$-space occur, corresponding also to a total momentum of

$$\vec{K} = \sum_{|\vec{k}|<|\vec{k}_F|} \vec{k} = 0. \tag{4.15}$$

These configurations correspond to the full occupation of all available degenerate energy levels, i.e. the full occupation of energy shells comparable to a full shell of atomic orbitals in the ground-state (noble gases). The first few closed-shell configurations are pictured in Fig. 4.6, which in 2D occur at the "magic" particle numbers $N = 2, 10, 18, 26, 42, \cdots$ for unpolarized systems. The energy for the noninteracting gas is shown in Fig. 4.4, labeled as $\eta = \infty$. We notice, that at particle numbers corresponding to fully occupied shells, the energy per particle features local minima. Strictly speaking, these configurations exist only in the noninteracting case, since states with higher momentum contribute immedi-

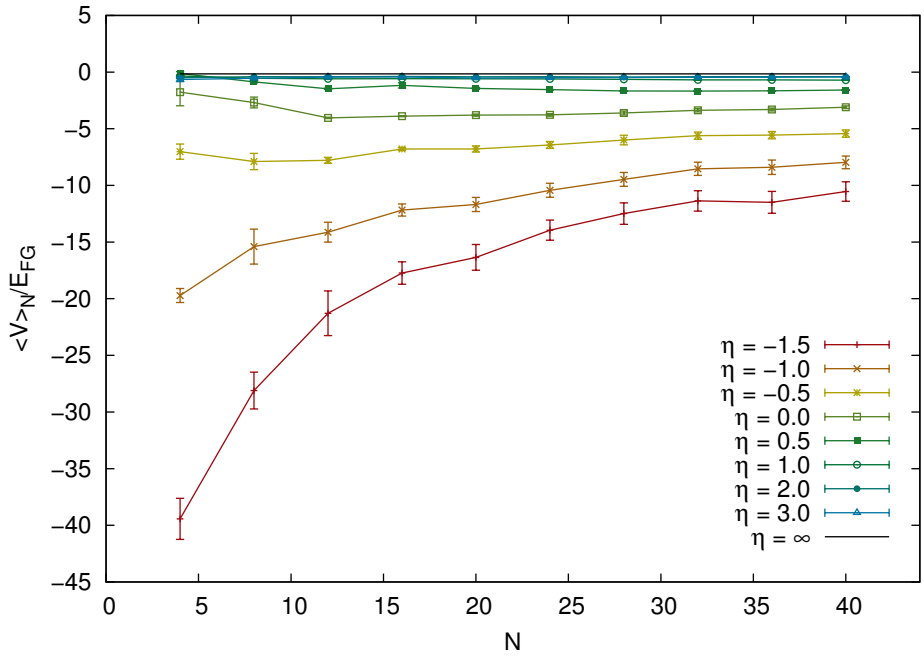

Figure 4.5: Expectation value of the density-density operator $\hat{V}$ for N = 4,8,12,...,40 fermions, in units of the ground-state energy of the noninteracting gas, for several values of the dimensionless coupling $\eta = -1.5, -1.0, \ldots, 3.0$, along with the noninteracting case $\eta \to \infty$. The solid black line shows $-1/(2\pi)$, which is the result in the noninteracting limit. (Reproduced from Ref. [49])

ately upon switching on the interaction. Nevertheless, for weakly bound systems in the BCS-regime, the remnants of the closed-shells are still visible in the EOS. For increasing interaction strength, however, this effect gets washed out entirely, as also observed in Ref. [75]. The lack of oscillations in the BEC-region is not surprising, since the structure of the wavefunction changes drastically and single-particle states are no longer eigenstates of the Hamiltonian.

4.3 Momentum distribution

In this section, we discuss our results for the momentum distribution n_k, which in 2D is defined as

$$n_k = \int_0^L d\vec{x}\, d\vec{x}' \rho_1(\vec{x}, \vec{x}') e^{i\vec{k}(\vec{x}-\vec{x}')}. \tag{4.16}$$

The momentum distribution is experimentally accessible and typically measured in ultracold-atoms experiments [84, 85]. Although such studies are necessarily conducted at finite temperature they are comparable, at least qualitatively, with the ground-state, which constitutes the limit for the lowest temperatures.
In Fig. 4.7, we show n_k for couplings across the entire BCS-BEC crossover with particle numbers $N = 12, 24$ and 36. While reasonable convergence was achieved for a 28×28 lattice for 12 particles, the grid size was increased to 32×32 for the latter cases. Ad-

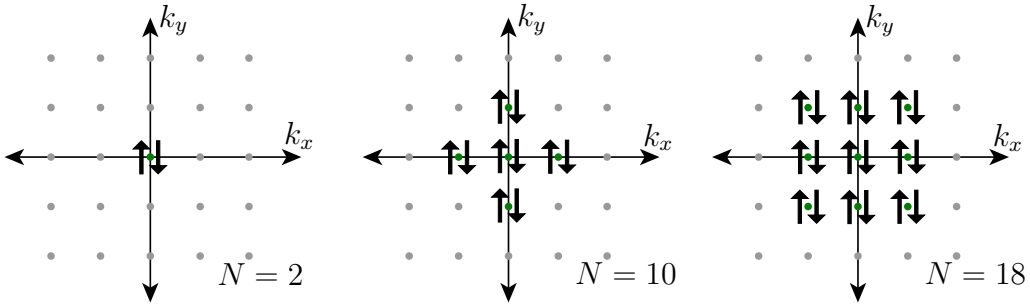

Figure 4.6: Lowest fully occupied energy shells at $N = 2, 10$ and 18.

ditionally, the curve for noninteracting Fermi gases, i.e. a step function with a drop at $|\vec{k}| = |\vec{k}_F|$, is shown. All results are shown as a function of $|\vec{k}|/|\vec{k}_F|$.
As expected, the weakly interacting curves in the BCS regime feature a relatively sharp drop, showing only minor modifications in the region $|k| \approx |k_\mathrm{F}|$ with respect to the non-interacting case. This indicates, that only particles near the Fermi surface participiate in the formation of pairs. Increasing the coupling leads to a broadening of the distribution, most pronounced in the strongly coupled BEC region, where the momentum distribution loses its features of a drop almost entirely. The wavefunction includes many $\vec{k}$-values, leading to a more localized form in real-space. In this limit, we no longer observe a Fermi surface, suggesting the formation of molecule-like bound pairs, i.e. composite bosons. A qualitatively similar trend for $n(\epsilon_\mathrm{K})$ with increasing interaction is found in Ref. [83] for the case of 2D Hubbard model wirh repulsive interaction in the high density limit of half-filling. In this study, the formation of bosonic bound pairs can be mapped to the formation of localized magnetic moments.
As the particle number increases, the effect of the interaction becomes smoother such that the momentum distribution "decays" slower with increasing coupling.
Additionally, the insets in Fig. 4.7 show the momentum distribution on a log-log scale, featuring the asymptotic behaviour as k approaches ∞. In the lowest populated systems, n_k takes on values below 10^{-6} which are subject to numerical inaccuracies in the weakest coupled cases. In principle, higher statistics could solve these problems. Fortunately, as coupling and particle density increase, these numerical issues vanish. In analogy to the 1D case, we perform a fit of the form

$$n_k \approx \frac{a}{|\vec{k}|^4} \tag{4.17}$$

to the tail of the distribution, where we cut off the values at $|\vec{k}|/|\vec{k}_F| \approx 1.8 - 2.2$, depending on the system size. The fitted functions are shown as solid lines in the insets of Fig. 4.7 and show very good agreement with the computed data.

4.3.1 Extrapolation to infinite β

The results discussed in the above, are extrapolated to infinite effective inverse temperature. Since no analytic form for the behaviour of the momentum distribution is known in

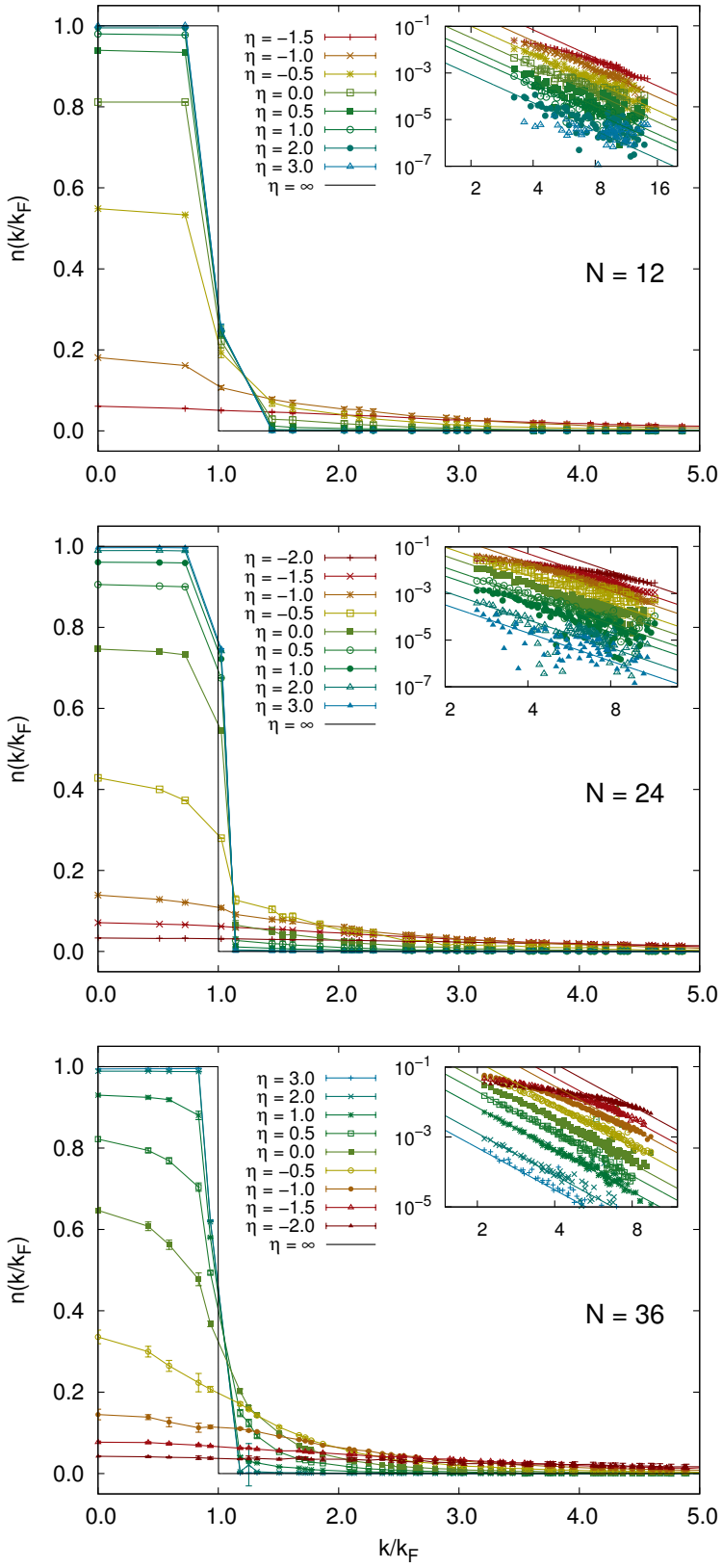

Figure 4.7: Momentum distributions as a function of $|\vec{k}|/|\vec{k}_F|$ for $N = 12, 24, 36$ unpolarized fermions with grid sizes of 28×28 for 12 particles and 32×32 otherwise. Inset: momentum distribution on a log-log scale, featuring the asymptotic $(|\vec{k}|/|\vec{k}_F|)^{-4}$ behaviour.

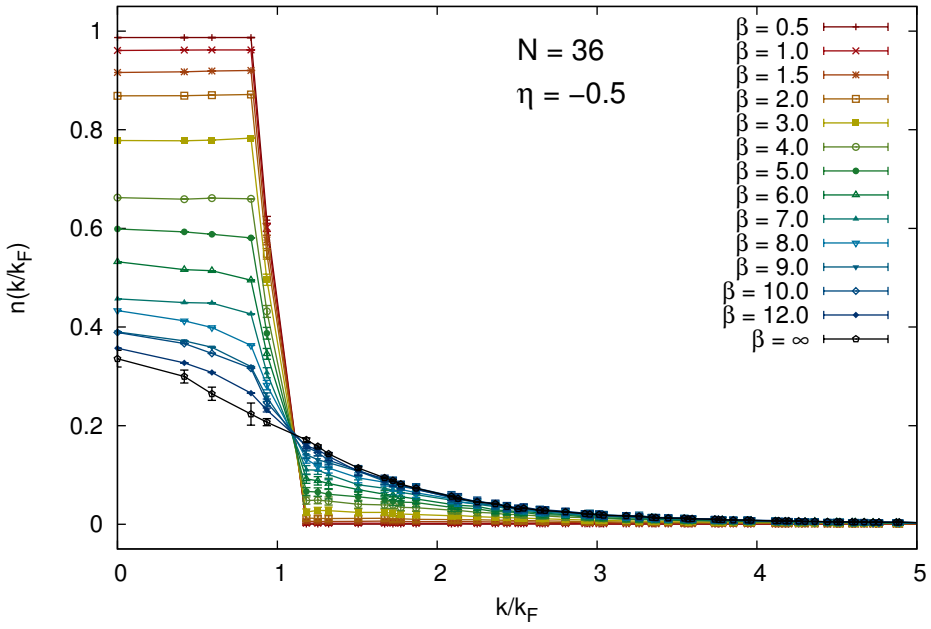

Figure 4.8: Momentum distribution extrapolated to infinite imaginary time β for $N = 36$ unpolarized fermions on a 32×32 lattice and at fixed dimensionless coupling $\eta = -0.5$. The black points corresponding to the extrapolated values in the ground-state.

the interacting case, we have chosen a Gaussian fit to catch the asymptotic behaviour. The extrapolation is shown in Fig. 4.8. We see, that for the convergence to the ground-state, values of $\beta \approx 8.0$ are needed, especially in the region $|\vec{k}| < |\vec{k}_F|$. As mentioned before, the rate of convergence could be improved by the use of improved trial states for the inital wavefunction as done in Refs. [75, 76].

4.4 One-body density matrix

Here, we present results for the one-body, equal-time density matrix $\rho_1(k_F r)$ for spin unpolarized fermions, defined as

$$\rho_1(\vec{x}, \vec{x}') = \langle \Omega | \, \hat{\psi}_\uparrow^\dagger(\vec{x}) \hat{\psi}_\uparrow(\vec{x}') \, | \Omega \rangle = \langle \Omega | \, \hat{\psi}_\downarrow^\dagger(\vec{x}) \hat{\psi}_\downarrow(\vec{x}') \, | \Omega \rangle \, . \tag{4.18}$$

The definition coincides with the one 1D, except for the fact that we now have to consider the vector-character of the coordinates.
Results for systems with a particle number of $N = 12, 24$ and 36 across the BCS-BEC crossover are presented. Again, we plotted the results for a 28×28 lattice in the first case and used a 32×32 grid otherwise. To eliminate the scale set by the density, we present our results as a function of $k_F r$. Due to the use of periodic boundary conditions, the investigated systems become translationally invariant. This allows us to use the distance

$$r = |\vec{x} - \vec{x}'| \tag{4.19}$$

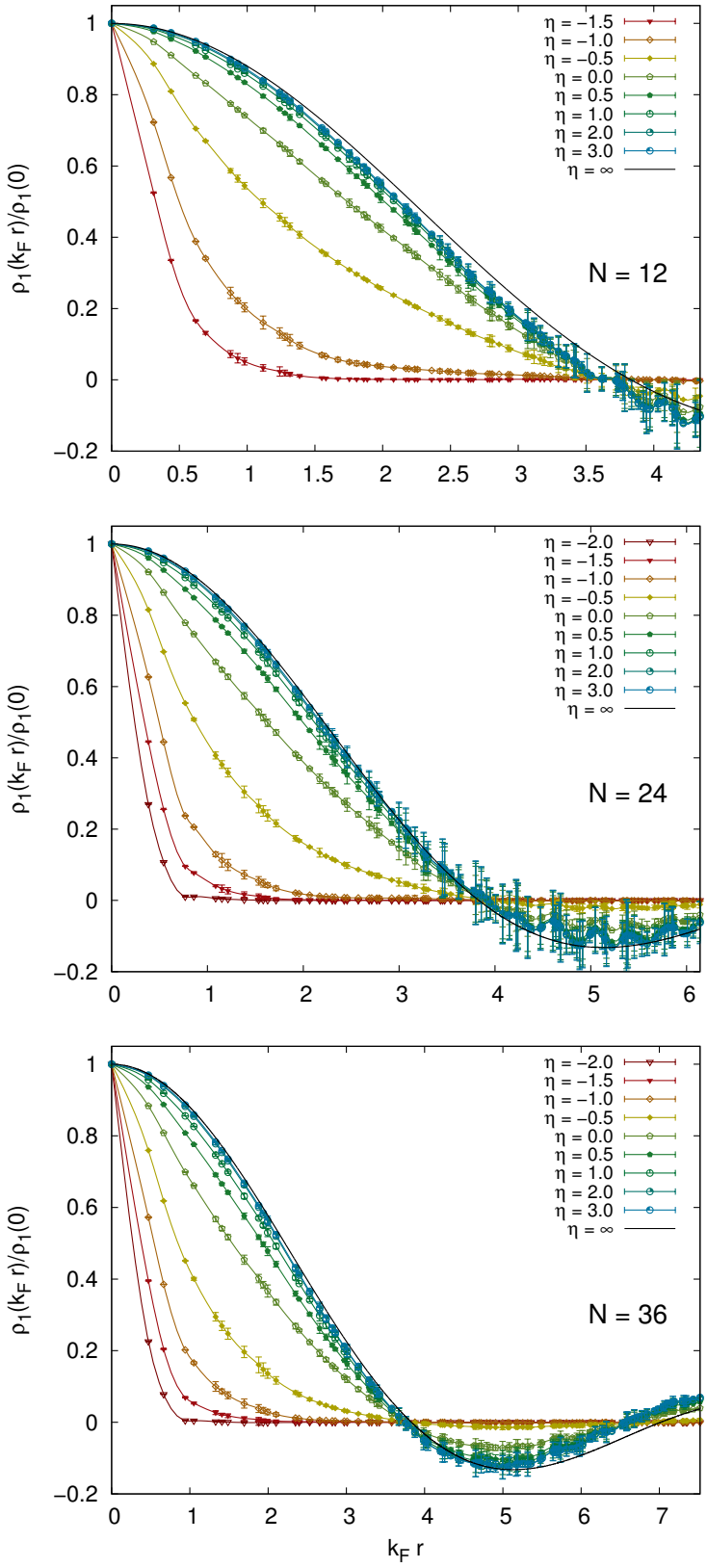

Figure 4.9: Single-particle density matrix ρ_1 as a function of $k_F r$ for $N = 12, 24, 36$ unpolarized fermions with grid sizes of 28×28 for 12 particles and 32×32 otherwise. The solid black line corresponds to the limit $\eta \to \infty$, i.e. the noninteracting case.

η	a	mean absolute deviation
-2.0	$0.45(3)$	0.001
-1.5	$0.44(3)$	0.002
-1.0	$0.42(3)$	0.004
-0.5	$0.27(6)$	0.03
0.0	$0.11(4)$	0.02
0.5	$0.06(4)$	0.02
1.0	$0.05(7)$	0.02
2.0	$0.0(1)$	0.02
3.0	$0.0(1)$	0.02

Table 4.3: Fit parameter a obtained by fitting Eq. (4.20) to the $N = 36$ data of Fig. 4.9, as a function of the dimensionless coupling η. Similar trends in a have been obtained for systems with a different number of particles, i.e. beyond the data of Fig. 4.9. (Reproduced from Ref. [49])

instead of considering results for every lattice point separately. Furthermore, we present the density matrix normalized to the respective value $\rho(r = 0)$ with the associated couplings.
By looking at Fig. 4.9, we observe the occurence of statistical noise for long-range correlations. To smoothen the curve, a three-point moving average was performed.
Since the single-particle density matrix is connected with the momentum distribution via Eq. (4.16), we can draw similar conclusions as discussed above. In the weakly interacting regime, the curves only slightly deviate from the noninteracting result, derived in App. B. As the coupling grows, the density matrix shows strong localization of particles with an exponential form for the highest coupling computed. This agrees well with the expectation in the infinitely attractive case, where one would expect the correlations to be a δ-distribution located at $r = 0$, as the composite-bosons would collapse in the same quantum-state.
The oscillations, associated with the existence of a well defined Fermi surface, become weaker with increasing interaction, until they vanish completely at the onset of the BEC phase around $\eta = -0.5$. This is another indication for the formation of tightly bound pairs, as it is expected in this limit and is in contrary to 1D systems, where the oscillations prevailed even in the highest coupled cases.
We can interpret the square of the inverse particle density $n^{-\frac{1}{2}}$ as the mean partricle spacing. Now we can think of the x-axis in Fig. 4.9 as a measure of how many average distances fit into the system. Although the curves for different particle contents coincide with this renormalization, the scale is extended for systems with higher density, therefore featuring more oscillations in the BCS limit.

Finally, in order to encode the short-ranged behaviour of the response, fits to the shown data were performed. The transition from the noninteracting case to the strongly coupled regime can be described by the introduction of a dimensionless parameter a, as

$$\rho_1(k_\mathrm{F} r) \approx 2e^{-a p_\mathrm{B} r} \frac{J_1(k_\mathrm{F} r)}{k_\mathrm{F} r}, \tag{4.20}$$

which describes the interpolation between the two limits. The second factor in Eq. (4.20) corresponds to the noninteracting result in the continuum limit, as derived in App. B. The Bessel function originates from the fact, that only states up to the Fermi wavevector are occupied in the noninteracting case. The first factor is motivated by the deeply bound state shown in Fig. 4.9. In this limit, correlations are expected to decay with the inverse binding momentum p_{B}. For nonzero interactions states with $k > k_{\mathrm{F}}$ are occupied and in the limit of infinite attraction, the momentum distribution approaches a constant, which corresonds to a delta peak for the correlation. Therefore, it is expected that for increasing coupling the form of the correlation is dicated by an increasing value of a. Numerical values, which underpin this behaviour, are provided in Tab. 4.3.

Chapter 5

Summary and Outlook

> *I call our world Flatland, not because we call it so, but to make its nature clearer to you, my happy readers, who are privileged to live in Space.*
>
> Edwin A. Abbott, [86].

Since our world is three-dimensional, naturally most of the experimental and theoretical effort was put forward to explain and investigate such materials and effects. Nevertheless, configurations exist where the motion of particles is confined effectively to lower dimensions and therefore behaviour generic to the reduced dimensionality is observed. Specifically, in solid-state physics, where the dynamics of the system is largely influenced by the motions of electrons, the explanation of these effects corresponds to the solution of a many-body problem. While in three-dimensions mean-field approaches yield reasonable results in several cases, lower dimensions are heavily influenced by quantum and thermal fluctuations, making mean-field approaches inapplicable and raising the need for more detailed calculations. In this work we have characterized the ground-state of systems with low dimensionality by the means of an auxiliary-field quantum Monte Carlo approach.
Although exact methods for the solution of one-dimensional Fermi gases exist, we have presented numerical results to describe the zero temperature behaviour. Specifically, we investigated the one- and two-body equal-time correlations for a broad range of couplings, showing a moderately increased particle localization for growing interaction strength. In order to further learn about the energetic structure in such systems, we investigated the momentum distribution across many particle numbers to show the effects of strong correlations on the "Fermi surface", which in 1D is constituted by two points. While the 1D results are of intrinsic interest, they were also used to benchmark our method for more challenging calculations carried out in two dimensions.
For the two-dimensional case, we set out to characterize the crossover from few- to many-body physics in the ground-state across a great range of interaction strengths. Typcially these systems are treated in the thermodynamic limit, neglecting the effects of few-body physics. To the best of our knowledge, the results presented in this work constitute the first determination of the few- to many-body crossover in two dimensions. We computed the equation of state for the ground-state energy, connecting the energy per particle to the particle content and showing the convergence to the thermodynamic limit, as calculated

in previous studies. Similarly, we provided such an equation of state for the interaction energy aming at learning about the short-ranged behaviour of these systems. We observe a domination of the dimer binding-energy in the strongly coupled regime, showing a clear hallmark of the formation of tightly bound pairs, i.e. composite bosons. This is further underpinned by the study of the momentum distribution as well as one-body correlations, which show an exponential form in the BEC limit as expected for a deeply bound molecular state.

In conclusion, we have provided a thorough study of the ground-state of one- and two-dimensional unpolarized Fermi gases on the lattice. Although the ovservables studied in this work already clearly show the effects of pairing in the BCS-BEC crossover a complete characterization of the system requires further studies. Several other quantities still need to be investigated, such as the condensate fraction, pair-momentum distribution, dynamic response functions etc. In order to fully characterize the phase-diagram of interacting Fermi gases in the ground-state, it would be also interesting to study the dependence on mass- and spin-imbalance as well as the influence of external trapping potentials. Combined with the extension to finite temperatures, the need for different approaches such as e.g. cluster and diagrammatic extensions of DMFT arises, with the goal to eventually nail down completely the peculiar behaviour of Fermi systems in reduced dimensions.

Appendices

A Ground state energy

In this appendix we provide a derivation for the decay of the interacting ground-state energy in imaginary time. In order to extract the ground-state energy, we can use the resulting functional form and apply a fit to the data.
The total energy at imaginary time β is given by

$$E(\beta) = \frac{\langle \Omega(\beta)| \hat{H} |\Omega(\beta)\rangle}{\langle \Omega(\beta)|\Omega(\beta)\rangle}, \tag{A.1}$$

where $\hat{H}$ is the Hamiltonian of the system and $|\Omega(\beta)\rangle$ denotes the projected state at fixed β. It is connected to the initial state $|\Omega_0\rangle$ via

$$|\Omega(\beta)\rangle = e^{-\beta\hat{H}} |\Omega(0)\rangle \equiv e^{-\beta\hat{H}} |\Omega_0\rangle , \tag{A.2}$$

so that the energy reads

$$E(\beta) = \frac{\langle \Omega_0| e^{-\beta\hat{H}} \hat{H} e^{-\beta\hat{H}} |\Omega_0\rangle}{\langle \Omega_0|e^{-2\beta\hat{H}}|\Omega_0\rangle} \tag{A.3}$$

An expansion of $|\Omega_0\rangle$ in occupation number basis states $|n\rangle$

$$|\Omega_0\rangle = \sum_n c_n |n\rangle \tag{A.4}$$

and insertion into the above expression yields:

$$E(\beta) = \frac{\sum_{nm} c_n c_m^* \langle m| e^{-\beta\hat{H}} \hat{H} e^{-\beta\hat{H}} |n\rangle}{\sum_{nm} c_n c_m^* \langle m| e^{-2\beta\hat{H}} |n\rangle}. \tag{A.5}$$

Applying the operators

$$E(\beta) = \frac{\sum_{nm} c_n c_m^* E_n e^{-\beta(E_n+E_m)} \langle m|n\rangle}{\sum_{nm} c_n c_m^* e^{-2\beta E_n} \langle m|n\rangle} \tag{A.6}$$

and exploiting the orthonormality property of the basis states $\langle n|m\rangle = \delta_n^m$ results in:

$$E(\beta) = \frac{\sum_{n=0}^{\infty} |c_n|^2 E_n e^{-2\beta E_n}}{\sum_{n=0}^{\infty} |c_n|^2 e^{-2\beta E_n}} \tag{A.7}$$

Further, we can separate the dominating factor in the sum, namely the ground-state energy, and rewrite the expression as

$$E(\beta) = \frac{E_0|c_0|^2 + \sum_{n=1}^{\infty} |c_n|^2 E_n e^{-2\beta(E_n-E_0)}}{|c_0|^2 + \sum_{n=1}^{\infty} |c_n|^2 e^{-2\beta(E_n-E_0)}}. \tag{A.8}$$

We can now assume that the factor $x_n \equiv e^{-\beta(E_n-E_0)}$ is small and hence perform an expansion

$$f(\vec{x}) = f(\vec{x})|_{\vec{x}=0} + \sum_{n=1}^{\infty} \left.\frac{\partial f(\vec{x})}{\partial x_n}\right|_{x_n=0} x_n + \sum_{nm} \mathcal{O}(x_n x_m) \tag{A.9}$$

which results to

$$E(\beta) = E_0 + \sum_{n=0}^{\infty} (E_n - E_0)\frac{|c_n|^2}{|c_0|^2} e^{-\beta(E_n-E_0)} + \sum_{nm} \mathcal{O}\left(e^{-\beta(E_m-E_0)} e^{-\beta(E_n-E_0)}\right). \tag{A.10}$$

Again, we can assume that the sum is dominated by the first term and write the approximate form

$$E(\beta) \approx E_0 + (E_1 - E_0)\frac{|c_1|^2}{|c_0|^2} e^{-\beta(E_1-E_0)}. \tag{A.11}$$

This form in general allows the calculation of the ground and first excited energies. Nevertheless, one has to be careful upon performing the fits, since the first excited energy is very sensitive to the decay constant, which is often hard to obtain within small error margin.

B Noninteracting one-body density matrix

Here we want to derive the noninteracting density matrices for 1D and 2D systems at zero temperature. The derivation is very similar in both cases and only differs in the evaluation of the occuring integrals.
Following the definition given in Sec. (1.3), we can write $\rho_1(x, x')$ as

$$\rho_1(\vec{x}, \vec{x}') = \langle \Omega_0 | \, \hat{\psi}^\dagger(\vec{x}')\hat{\psi}(\vec{x}) \, | \Omega_0 \rangle \, . \tag{B.1}$$

With the vacuum state $|0\rangle$ we can write the noninteracting ground state:

$$\rho_1(\vec{x}, \vec{x}') = \langle 0 | \prod_{|\vec{k}|<|\vec{k}_F|} \hat{a}_{\vec{k}}^\dagger \hat{\psi}^\dagger(\vec{x}')\hat{\psi}(\vec{x}) \prod_{|\vec{k}'|<|\vec{k}_F|} \hat{a}_{\vec{k}'}^\dagger \, | 0 \rangle \, . \tag{B.2}$$

Equivalently, in momentum-space we write

$$\rho_1(\vec{x}, \vec{x}') = \langle 0 | \prod_{|\vec{k}|<|\vec{k}_F|} \hat{a}_{\vec{k}}^\dagger \sum_{\vec{q}\vec{q}'} \phi_{\vec{q}'}^*(\vec{x}')\phi_{\vec{q}}(\vec{x}) \hat{a}_{\vec{q}'}^\dagger \hat{a}_{\vec{q}} \prod_{|\vec{k}|'<|\vec{k}_F|} \hat{a}_{\vec{k}'}^\dagger \, | 0 \rangle \, . \tag{B.3}$$

After some anticommutator-arithmetic, we finally arrive at the sum

$$\rho_1(\vec{x}, \vec{x}') = \sum_{|\vec{k}|<|\vec{k}_F|} \phi_{\vec{k}}^*(\vec{x}')\phi_{\vec{k}}(\vec{x}). \tag{B.4}$$

B.1 One dimension

In 1D we can approximate the above sum with an integral considering the correction factor $L/2\pi$ to account for the volume:

$$\rho_1(x, x') \approx \frac{L}{2\pi} \int_{-k_F}^{k_F} dk\ \phi_k^*(x')\phi_k(x). \tag{B.5}$$

In free system, represented by the use of periodic boundary conditions, the single-particle contributions are given by plane waves. Therefore the integrand can be explicitly written and the integral becomes

$$\rho_1(|x - x'|) = \frac{L}{2\pi} \int_{-k_F}^{k_F} dk\ e^{ik(x'-x)}. \tag{B.6}$$

We are able to evaluate this integral to

$$\rho_1(k_F r) = \frac{2}{|x' - x|} \sin\left(k_F |x' - x|\right) \tag{B.7}$$

and use $|x' - x| = r$ to obtain the final form as

$$\rho_1(k_F r) = \frac{N}{2} \frac{\sin\left(k_F r\right)}{k_F r}. \tag{B.8}$$

B.2 Two dimensions

In the 2D case the sum can be approximated by

$$\rho_1(\vec{x}, \vec{x}') \approx \left(\frac{L}{2\pi}\right)^2 \int_{|\vec{k}|<|\vec{k}_F|} d^2k\ \phi_{\vec{k}}^*(x')\phi_{\vec{k}}(x). \tag{B.9}$$

The evaluation of this expression is more subtle since we have to consider the vector character of the integral kernel. We need to rewrite the integral to

$$\rho_1(r) = \left(\frac{L}{2\pi}\right)^2 \int_0^{k_F} dk \left[k \int_0^{2\pi} d\varphi\ e^{ikr\cos\varphi}\right]. \tag{B.10}$$

where we used $r = |\vec{x}' - \vec{x}|$. The inner integral corresponds to a representation of *Bessel functions* $J_n(x)$ of order n, up to a normalization. We get

$$\rho_1(r) = \frac{L^2}{2\pi} \int_0^{k_F} dk\ kJ_0(kr) \tag{B.11}$$

which leaves with the evaluation of the k-integral. By using the properties of Bessel functions, and integrating by parts, we arrive at the final form

$$\rho_1(r) = N \frac{J_1(k_F r)}{k_F r}. \tag{B.12}$$

C Suzuki-Trotter decomposition

In many problems of numerical physics we encounter the problem of evaluating an exponential operator as e.g. in the partition function introduced in Sec. (1.2)

$$\mathcal{Z} = \mathrm{Tr}[e^{-\beta\hat{H}}] = \mathrm{Tr}[e^{-\beta(\hat{T}+\hat{V})}], \tag{C.1}$$

where $\hat{T}$ and $\hat{V}$ correspond to the kinetic and interaction part of the Hamiltonian, respectively. These two operators do not commute in general, which makes the use of the simple form

$$e^{-\beta(\hat{T}+\hat{V})} = e^{-\beta\hat{T}}e^{-\beta\hat{V}} \tag{C.2}$$

impossible. In fact, by expanding these two exponential operators, we can calculate the error if we use Eq. (C.2) as an approximation:

$$e^{-\beta(T+V)} = I - \beta(T+V) + \frac{\beta^2}{2}(T+V)^2 + \mathcal{O}(\beta^3) \tag{C.3a}$$

$$= I - \beta(T+V) + \frac{\beta^2}{2}(T^2 + TV + VT + V^2) + \mathcal{O}(\beta^3) \tag{C.3b}$$

$$e^{-\beta T}e^{-\beta V} = \left(I - \beta T + \frac{\beta^2}{2}T^2 + \mathcal{O}(\beta^3)\right)\left(I - \beta V + \frac{\beta^2}{2}V^2 + \mathcal{O}(\beta^3)\right) \tag{C.4a}$$

$$= I - \beta(T+V) + \frac{\beta^2}{2}(T^2 + 2TV + V^2) + \mathcal{O}(\beta^3) \tag{C.4b}$$

Comparing these two expressions, we note that in the latter T always occurs before V, whereas switched terms occur in the former case. Carrying out the calculation, we obtain

$$e^{-\beta T}e^{-\beta V} = e^{-\beta(T+V)+\frac{\beta^2}{2}[T,V]+\mathcal{O}(\beta^3)} \tag{C.5}$$

which corresponds to the well known *Trotter-formula* [87]

$$e^{-\beta T}e^{-\beta V} = e^{-\beta(T+V)+\mathcal{O}(\beta^2)}. \tag{C.6}$$

In order to keep the approximation error at a minimum, the expansion parameter β should be as small as possible. Introducing the *Trotter-number* n, we can discretize the expansion parameter β into slices

$$\left(e^{\frac{\beta}{n}T}e^{\frac{\beta}{n}V}\right)^n = e^{x(T+V)+\mathcal{O}\frac{\beta^2}{n}} \tag{C.7}$$

for which the correction term vanishes in the limit $n \to \infty$. Although this is already a form one could use computationally, it would be more feasible if the correction term vanishes faster than $\mathcal{O}(\frac{\beta^2}{n})$. In order to do this, we can wite the general form of such a decomposition, as done in Ref. [88]:

$$e^{-\beta(T+V)} = e^{-\beta p_1 T}e^{-\beta p_2 V}\cdots e^{-\beta p_m V} + \mathcal{O}(\beta^{m+1}). \tag{C.8}$$

The simplest improvement is obtained by the expansion to the order of $m = 2$ followed by equating the coefficients. We get

$$e^{-\beta(T+V)} = e^{-\frac{\beta}{2}T} e^{-\beta V} e^{-\frac{\beta}{2}T} + \mathcal{O}(\beta^3), \tag{C.9}$$

which is the approximation we use in this work.

D Hubbard-Stratonovich transformation

The *Hubbard-Stratonovich (HS) transformation* [89, 90] is based on the expression

$$e^{\frac{1}{2}A^2} = \sqrt{2\pi} \int d\sigma \; e^{-\frac{1}{2}\sigma^2 - \sigma A}, \tag{D.1}$$

where A is an arbitrary quantum-mechanical operator and σ constitutes a newly introcudced *auxiliary field*. It allows us to rewrite the Hamiltonian from Eq. (2.23) to a more suitable expression, containing only one-body operators, diagonalizable in real-space. The operator of interest is given by the exponential

$$e^{-\Delta\tau \hat{V}} = e^{-\Delta\tau g \sum_i n_{\uparrow,i} n_{\downarrow,i}} = \prod_i e^{-\Delta\tau g n_{\uparrow,i} n_{\downarrow,i}}, \tag{D.2}$$

where the summation (product) streches over all lattice sites i and the density at a lattice site x_i is written as $n_{s,i}$. Further, we define

$$\hat{V}_i \equiv g \; n_{\uparrow,i} n_{\downarrow,i} \tag{D.3}$$

and write

$$e^{-\Delta\tau \hat{V}} = \prod_i e^{-\Delta\tau \hat{V}_i}. \tag{D.4}$$

In order for Eq. (D.1) to be of use, we need to rewrite the interaction into a quadratic form. Therefore we write

$$n_\uparrow n_\downarrow = -\frac{1}{2}(n_\uparrow - n_\downarrow)^2 + \frac{1}{2}(n_\uparrow + n_\downarrow), \tag{D.5}$$

which holds since the value of the fermionic density is either zero or one. Inserting Eq. (D.5) into Eq. (D.3) yields

$$e^{-\Delta\tau \hat{V}_i} = e^{-\frac{\Delta\tau g}{2}(n_{\uparrow,i} + n_{\downarrow,i})} \; e^{\frac{1}{2}[\sqrt{\tau g}(n_{\uparrow,i} - n_{\downarrow,i})]^2}. \tag{D.6}$$

The first factor in this expression is already in the desired one-body form, whereas the square in the second factor produces quadratic density terms. We can use Eq. (D.1) and rewrite it to

$$e^{-\Delta\tau \hat{V}_i} = \sqrt{2\pi} \int d\sigma_i \; e^{-\frac{1}{2}\sigma_i^2} \; e^{-\frac{\Delta\tau g}{2}(n_{\uparrow,i} + n_{\downarrow,i})} \; e^{\sqrt{\tau g}(n_{\uparrow,i} - n_{\downarrow,i})\sigma_i}. \tag{D.7}$$

Now, any occuring density operator only occurs linearly, which we can diagonalize separately in real-space. We further rewrite the above expression to separate the contributions from different spin-species to

$$e^{-\Delta\tau\hat{V}_i} = \sqrt{2\pi}\int d\sigma_i \; e^{-\frac{1}{4}\sigma_i^2-\left(\frac{\Delta\tau g}{2}-\sqrt{\tau g}\sigma_i\right)n_{\uparrow,i}} \; e^{-\frac{1}{4}\sigma_i^2-\left(\frac{\Delta\tau g}{2}+\sqrt{\tau g}\sigma_i\right)n_{\downarrow,i}} \tag{D.8}$$

and with

$$\hat{V}_{\uparrow,i} = e^{-\frac{1}{4}\sigma_i^2-\left(\frac{\Delta\tau g}{2}-\sqrt{\tau g}\sigma_i\right)n_{\uparrow,i}} \tag{D.9a}$$

$$\hat{V}_{\downarrow,i} = e^{-\frac{1}{4}\sigma_i^2-\left(\frac{\Delta\tau g}{2}+\sqrt{\tau g}\sigma_i\right)n_{\downarrow,i}}, \tag{D.9b}$$

we arrive at

$$e^{-\Delta\tau\hat{V}_i} = \sqrt{2\pi}\int d\sigma_i \; e^{\hat{V}_{\uparrow,i}} \; e^{\hat{V}_{\downarrow,i}}. \tag{D.10}$$

Finally, we collect the factors of every lattice site into one integral and obtain

$$e^{-\Delta\tau\hat{V}} = (2\pi)^{\frac{N_x^d}{2}}\int \mathcal{D}\sigma \; e^{-\Delta\tau\hat{V}_{\uparrow,\sigma}} \; e^{-\Delta\tau\hat{V}_{\downarrow,\sigma}}, \tag{D.11}$$

where N_x^d is the number of lattice sites and the integration variable is written as as

$$\mathcal{D}\sigma = \prod_i d\sigma_i. \tag{D.12}$$

Eq. (D.11) corresponds to the interaction operator at a given time-slice. To produce the full interaction operator, one needs to combine such an integration for every step in the temporal latiice, as introduced in Sec. 2.2.

Bibliography

[1] R.D. Mattuck. A Guide to Feynman Diagrams in the Many-Body Problem. *Dover Books on Physics, Dover Publications*, **2nd** edition, 1992.

[2] P. Drude. Zur Elektronentheorie der Metalle. *Ann. Phys.*, **306**(3):566-613, 1900.

[3] P. Hohenberg, W. Kohn. Inhomogeneous Electron Gas. *Phys. Rev.*, **136**(28):B864, 1964.

[4] W. Kohn, L.J. Sham. Self-Consistent Equations Including Exchange and Correlation Effects. *Phys. Rev.*, **140**(4A):A1133, 1965.

[5] A. Georges, G. Kotliar, W. Krauth, M.J Rozenberg. Dynamical mean-field theory of strongly correlated fermion systems and the limit of infinite dimensions. *Rev. Nod. Phys.*, **68**(1):13-125, 1996.

[6] K. Held. Electronic structure calculations using dynamical mean field theory. *Adv. Phys.*, **56**(6):829-926, 2007.

[7] W. Metzner, D. Vollhardt. Correlated Lattice Fermions in $d = \infty$ Dimensions. *Phys. Rev. Lett.*, **62**(3):324-327, 1989.

[8] N.F. Mott. The Basis of the Electron Theory of Metals, with Special Reference to the Transition Metals. *Proc. Phys. Soc.*, **62**(7):416, 1949.

[9] M. Imada, A. Fujimori, Y. Tokura. Metal-insulator transitions. *Rev. Mod. Phys.*, **70**(4):1039-1263, 1998.

[10] M.H. Anderson, J.R. Ensher, M.R. Matthews, C.E. Wieman, E.A. Cornell. Observation of Bose-Einstein Condensation in a Dilute Atomic Vapor. *Science*, **296**(5221):198-201, 1995.

[11] C.C. Bradley, C.A. Sackett, J.J. Tollet, R.G. Hulet. Evidence of Bose-Einstein Condensation in an Atomic Gas with Attractive Interactions. *Phys. Rev. Lett.*, **75**(9):1687-1690, 1995.

[12] K.B. Davis, M.O. Mewes, M.R. Andrews, N.J. van Druten, D.S. Durfee, D.M. Kurn, W. Ketterle. *Bose-Einstein Condensation in a Gas of Sodium Atoms*, **75**(22):3969-3973, 1995.

[13] F.H.L Essler, H. Frahm, F. Göhmann, A. Klümper, V.E. Korepin. The one-dimensional Hubbard model. *Cambridge University Press*, Cambridge, 2005.

[14] L. Onsager. Crystal Statistics. I. A Two-Dimensional Model with an Order-Disorder Transition. *Phys. Rev.*, **65**(3-4):117-149, 1944.

[15] D.A. McQuarrie. Statistical Mechanics. *University Science Books*, Sausalito, 2000.

[16] X.J. Liu, H. Hu, P.D. Drummond. Three attractively interacting fermions in a harmonic trap: Exact solution, ferromagnetism, and high-temperature thermodynamics. *Phys. Rev. A*, **82**(2):023619, 2010.

[17] X.J. Liu, H. Hu, P.D. Drummond. Exact few-body results for strongly correlated quantum gases in two dimensions. *Phys. Rev. A*, **82**(2):054524, 2010.

[18] R.G. Littlejohn, M. Cargo. Multidimensional discrete variable representation bases: Sinc functions and group theory. *J. Chem. Phys.*, **116**:7350, 2002.

[19] R.G. Littlejohn, M. Cargo, T. Carrington Jr., K.A. Mitchell. A general framework for discrete variable representation basis sets. *J. Chem. Phy.*, **116**:8691, 2002.

[20] A. Bulgac, J.E. Drut, P. Magierski. Quantum Monte Carlo simulations ot the BCS-BEC crossover at finite temperature. *Phys. Rev. A*, **78**(2):023625, 2008.

[21] H. Feshke, R. Schneider, A. Weiße. Computational Many-Particle Physics. *Springer*, **1st** edition, 2008.

[22] S. Tan. Energetics of a strongly correlated Fermi gas. *Ann. Phys.*, **323**(12):2952-2970, 2008.

[23] S. Tan. Large momentum part of a strongly correlated Fermi gas. *Ann. Phys.*, **323**(12):2971-2986, 2008.

[24] S. Tan. Large momentum part of a strongly correlated Fermi gas. *Ann. Phys.*, **323**(12):2987-2990, 2008.

[25] E. Braaten, in The BCS-BEC Crossover and the Unitary Fermi Gas, edited by W. Zwerger *Springer-Verlag*, 2012).

[26] D.P. Landau, K. Binder. A Guide to Monte Carlo Simulations in Statistical Physics. *Cambridge University Press*, **3rd** edition, 2009.

[27] N. Metropolis, A. W. Rosenbluth, M. N. Rosenbluth, a. H. Teller, and E. Teller. Equation of state calculations by fast computing machines. *Journ. Chem. Phys.*, **21**(6):1087-1092, 1970.

[28] W.K. Hastings. Monte carlo methods using markov chains and their applications. *Biometrika*, **57**(1):97-109, 1970.

[29] A.N. Rubtsov, V.V. Savkin, A.I. Lichtenstein. Continuous-time quantum Monte Carlo method for fermions. *Phys. Rev. B*, **72**(3):035122, 2005.

[30] A. Bulgac, J.E. Drut, P. Magierski. Quantum Monte Carlo simulations of the BCS-BEC crossover at finite temperature. *Phys. Rev. A*, **78**(2):023625, 2008.

[31] J.E. Drut and A.N. Nicholson. Lattice methods for strongly interacting many-body systems. *J. Phys. G*, **40**:043101 (2013).

[32] S. Duane, A.D. Kennedy, B.J. Pnedleton, D. Roweth. Hybrid Monte Carlo. *Phys. Lett. B*,**195**(2):216-222, 1987.

[33] M. Troyer, U. Wiese. Computational Complexity and Fundamental Limitations to Fermionic Quantum Monte Carlo Simulations. *Phys. Rev. Lett.*, **94**(17):170201, 2005.

[34] D. Roscher, J. Braun, J. Chen, J.E. Drut. Fermi gases with imaginary mass imbalance and the sign problem in Monte-Carlo calculations. *Journ. Phys. G*, **41**(5):055110, 2014.

[35] J. Sólyom. The Fermi gas model of one-dimensional conductors. *Adv. Phys.*, **28**(2):201-303, 1979.

[36] H. Feshbach. Unified theory of nuclear reactions. *Ann. Phys.*, **5**(4):357-390, 1958. H.Feshbach. A unified theory of nuclear reactions II. *Ann. Phys.*, **19**(2):287-313, 1962.

[37] H. Moritz, T. Stöferle, K. Günter, M. Köhl, T. Esslinger. Confinement Induced Molecules in a 1D Fermi Gas. *Phys. Rev. Lett.*, **94**(21):210401, 2005.

[38] F.D.M. Haldane. 'Luttinger liquid theory' of one-dimensional quantum fluids. I. Properties of the Luttinger model and their extension to the general 1D interacting spinless Fermi gas. *J. Phys. C*, **14**(19):2585, 1981.

[39] J. Voit. One-dimensional Fermi liquids. *Rep. Prog. Phys.*, **58**(9):977, 1995.

[40] H. Bethe. Zur Theorie der Metalle. *Z. Phys.*, **73**(3):205-226, 1931.

[41] C.N. Yang. Some exact results for the many-body problem in one dimension with repulsive delta-function interaction. *Phys. Rev. Lett.*, **19**:1312 (1967).

[42] X.W. Guan, M.T. Batchelor, C. Lee. Fermi gases in one dimension: From Bethe ansatz to experiments. *Rev. Mod. Phys.*, **85**(4):1633-1691, 2013.

[43] L. Rammelmüller, W.J. Porter, A.C. Loheac, J.E. Drut. Few-fermion systems in one dimension: Ground- and excited-state energies and contacts. *Phys. Rev. A*, **92**(1):013613, 2015.

[44] C.E. Berger, E.R. Anderson, J.E. Drut. Energy, contact, and density profiles of one-dimensional fermions in a harmonic trap via nonuniform-lattice Monte Carlo calculations. *Phys. Rev. A*, **91**(5):053818, 2015.

[45] D. Roscher, J. Braun, J.E. Drut. Inhomogeneous phases in one-dimensional mass- and spin-imbalanced Fermi gases. *Phys. Rev. A*, **89**(6):063609, 2014.

[46] A.C. Loheac, J. Braun, J.E. Drut, D. Roscher. Thermal equation of state of polarized fermions in one dimension via complex chemical potentials. *Phys. Rev. A*, **92**(6):063609, 2015.

[47] X. Yin, X. Guan, M.T. Batchelor, S. Chen. Effective super Tonks-Girardeau gases as ground states of strongly attractive multicomponent fermions. *Phys. Rev. A*, **83**(1):013602, 2011.

[48] J.E. Drut, T.A. Lähde, T. Timour. Momentum Distribution and Contact of the Unitary Fermi Gas. *Phys. Rev. Lett.*, **106**(20):205302, 2011.

[49] L. Rammelmüller, W.J. Porter, J.E. Drut. Ground state of the two-dimensional attractive Fermi gas: Essential properties from few to many body. *Phys. Rev. A*, **93**(3):033639, 2016.

[50] M.G. Ries, A.N. Wenz, G. Zürn, L. Bayha, I. Boettcher, D. Kedar, P.A. Murthy, M. Neidig, T. Lompe, S. Jochim. Observation of Pair Condensation in the Quasi-2D BEC-BCS Crossover. *Phys. Rev. Lett.*, **114**(23):230401, 2015.

[51] I. Bloch, J. Dalibard, W. Zwerger. Many-body physics with ultracold gases. *Rev. Mod. Phys.*, **80**(3):885-964, 2008.

[52] N.D. Mermin, H. Wagner. Absence of Ferromagnetism or Antiferromagnetism in One- or Two-Dimensional Isotropic Heisenberg Models. *Phys. Rev. Lett.*, **17**(22):1133-1136, 1966.

[53] P.C. Hohenberg. Existence of Long-Range Order in One and Two Dimensions. *Phys. Rev.*, **158**(2):383-386, 1967.

[54] S. Coleman. There are no Goldstone bosons in two dimensions. *Comm. Math. Phys.*, **31**(4):259-264, 1973.

[55] J.M. Kosterlitz, D.J. Thouless. Ordering, metastability and phase transitions in two-dimensional systems. *Journ. Phys. C*, **6**(7):1181, 1973.

[56] V.L. Berezinskii. Destruction of Long-range Order in One-dimensional and Two-dimensional Systems Possessing a Continuous Symmetry Group. *JETP*, **34**(3):1144, 1972.

[57] Z. Hadzibabic, P. Kruger, M. Cheneau, B. Battelier, J. Dalibard. Berezinskii-Kosterlitz-Thouless crossover in a trapped atomic gas. *Nature*, **441**(7097):1118-1121, 2006.

[58] S.A. Kivelson, I.P. Bindloss, E. Fradkin, V. Oganesyan, J.M. Tranquada, A. Kapitulnik, C. Howald. How to detect fluctuating stripes in the high-temperature superconductors. *Rev. Mod. Phys.*, **75**(4):1201-1241, 2003.

[59] M. Klawunn, Equation of state and Kosterlitz-Thouless transition temperature in two-dimensional Fermi gases: An analytical approach. *arXiv*:1511.05123, 2016.

[60] W. Zhang, G. D. Lin, L.M. Duan. BCS-BEC crossover of a quasi-two-dimensional Fermi gas: The significance of dressed molecules. *Phys. Rev. a*, **77**(6):063613, 2008.

[61] M. Randeria, J.M. Duan, L.Y. Shieh. Bound states, Cooper pairing, and Bose condensation in two dimensions. *Phys. Rev. Lett.*, **63**(9):981-984, 1989.

[62] G. Keller, K. Held, V. Eyert, D. Vollhardt, V.I. Anisimov. Electronic structure of paramagnetic V2O3: Strongly correlated metallic and Mott insulating phase. *Phys. Rev. B*, **70**(20):205116, 2004.

[63] A. Toschi, M. Capone, C. Castellani. Energetic balance of the superconducting transition across the BCS—Bose Einstein crossover in the attractive Hubbard model. *Phys. Rev. B*, **72**(23):235118, 2005.

[64] G. Kotliar, S. Savrasov, G. Palsson, G. Biroli. Cellular Dynamical Mean Field Approach to Strongly Correlated Systems. *Phys. Rev. Lett.*, **86**(18):186401, 2001.

[65] A.I. Lichtenstein M.I. Katsnelson. Antiferromagnetism and d-wave superconductivity in cuprates: A cluster dynamical mean-field theory. *Phys. Rev. B*, **62**(14):R9283, 2000.

[66] T. Maier, M. Jarrell, T. Pruschke, M.H. Hettler. Quantum cluster theories. *Rev. Mod. Phys.*, **77**(3):1027, 2005.

[67] A. Toschi, A.A. Katanin, K. Held. Dynamical vertex approximation: A step beyond dynamical mean-field theory. *Phys. Rev. B*, **75**(4):045118, 2007.

[68] H. Kusunose. Influence of Spatial Correlations in Strongly Correlated Electron Systems: Extension to Dynamical Mean Field Approximation. *J. Phys. Soc. Jpn.*, **75**:054713, 2006.

[69] A.N. Rubtsov, M.I. Katsnelson, A.I. Lichtenstein. Dual fermion approach to nonlocal correlations in the Hubbard model. *Phys. Rev. B*, **77**(3):033101, 2008.

[70] C. Slezak, M. Jarrell, T. Maier, J. Deisz. Multi-scale Extensions to Quantum Cluster Methods for Strongly Correlated Electron Systems. *J. Phys: Condens. Matter*, **21**(17):435604, 2009.

[71] A. Valli, G. Sangiovanni, O. Gunnarsson, A. Toschi. Dynamical Vertex Approximation for Nanoscopic Systems. *Phys. Rev. Lett*, **104**(24):246402, 2010.

[72] A Toschi, G. Rohringer, A. Katanin, K. Held. Ab initio calculations with the dynamical vertex approximation. *Ann. Phys.*, **523**(8-9):629, 2011.

[73] C. Taranto, S. Andergassen, J. Bauer, K. Held, A. Katanin, W. Metzner, G. Rohringer, A. Toschi. From Infinite to Two Dimensions through the Functional Renormalization Group. *Phys. Rev. Lett.*, **112**(19):196402, 2014.

[74] G. Bertaina, S. Giorgini. BCS-BEC Crossover in a Two-Dimensional Fermi Gas. *Phys. Rev. Lett.*, **106**(11):110403, 2011.

[75] A. Galea, H. Dawkins, S. Gandolfi, A. Gezerlis. Diffusion Monte Carlo study of strongly interacting two-dimensional Fermi gases. *Phys. Rev. A*, **93**(2):023602, 2016.

[76] H. Shi, S. Chiesa, S. Zhang. Ground-state properties of strongly interacting Fermi gases in two dimensions. *Phys. Rev. A.*, **92**(3):033603, 2015.

[77] E. R. Anderson, J. E. Drut. Pressure, Compressibility, and Contact of the Two-Dimensional Attractive Fermi Gas. *Phys. Rev. Lett.*, **115**(11):115301, 2015.

[78] X.J. Liu, H. Hu, P.D. Drummond. Exact few-body results for strongly correlated quantum gases in two dimensions. *Phys. Rev. B*, **82**(5):054524, 2010.

[79] M. Barth, J. Hofmann. Pairing effects in the nondegenerate limit of the two-dimensional Fermi gas. *Phys. Rev. A*, **89**(1):013614, 2014.

[80] G. E. Astrakharchik, J. Boronat, J. Casulleras, S. Giorgini. Equation of State of a Fermi Gas in the BEC-BCS Crossover: A Quantum Monte Carlo Study. *Phys. Rev. Lett*, **93**(20):200404, 2004.

[81] C. Langmack, M. Barth, W. Zwerger, E. Braaten. Clock Shift in a Strongly Interacting Two-Dimensional Fermi Gas. *Phys. Rev. Lett.*, **108**(6):060402, 2012.

[82] L. Viverit, S. Giorgini, L.P. Pitaevskii, S. Stringari. Momentum distribution of a trapped Fermi gas with large scattering length. *Phys. Rev. A*, **69**(1):013697, 2004.

[83] G. Rohringer, A. Toschi. Impact of non-local correlations over different energy scales: A Dynamical Vertex Approximation study. arXiv:1604.08748.

[84] M.G. Ries, A.N. Wenz, G. Zürn, L. Bayha, I. Boettcher, D. Kedar, P.A. Murthy, M. Neidig, T. Lompe, S. Jochim. Observation of Pair Condensation in the Quasi-2D BEC-BCS Crossover. *Phys. Rev. Lett.*, **114**(23):230401, 2015.

[85] C.A. Regal, M. Greiner, S. Giorgini, M. Holland, D.S. Jin. Momentum Distribution of a Fermi Gas of Atoms in the BCS-BEC Crossover. *Phys. Rev. Lett.*, **95**(25):250404, 2005.

[86] E.A. Abbott. Flatland: A Romance in Many Dimensions. *Seeley & Co.*, London, 1884.

[87] H.F. Trotter, On the product of semigroups of operators, *Proc. Amer. Math. Soc.*, **10**:545-551, 1959). 545-551.

[88] M. Suzuki. Fractal decomposition of exponential operators with applications to many-body theories and Monte Carlo simulations. *Phys. Lett. A*, **146**(6):319-323, 1990.

[89] J. Hubbard. Calculation of Partition functions. *Phys. Rev. Lett.*, **3**(2):77-78, 1959.

[90] J.E. Hirsch. Discrete Hubbard-Stratonovich transformation for fermion lattice models. *Phys. Rev. B*, **28**(7):4059-4061, 1983.